

Low-temperature T-linear resistivity in the strange-metal phase of overdoped cuprate superconductors due to umklapp scattering from a spin excitation

Xingyu Ma,^{*} Minghuan Zeng,^{*} Zhangkai Cao, and Shiping Feng[†]
Department of Physics, Beijing Normal University, Beijing 100875, China

The strange-metal phase of overdoped cuprate superconductors exhibits a linear in temperature resistivity in low temperatures, however, the origin of this remarkable anomaly is still not well understood. Here the linear temperature dependence of the resistivity in the strange-metal phase of overdoped cuprate superconductors is investigated. The momentum dependence of the transport scattering rate is arisen from the electron umklapp scattering mediated by the spin excitation, and is employed to calculate the resistivity by making use of the Boltzmann equation. It is shown that the resistivity is mainly dominated by the antinodal and nodal umklapp scattering. In particular, a very low temperature T_{scale} scales with Δ_p^2 , where Δ_p is the minimal umklapp vector at the antinode. In the low temperature above T_{scale} , the resistivity is linear in temperature with a coefficient that decreases with the increase of doping, however, in the far lower temperature below T_{scale} , the resistivity is instead quadratic in temperature. The theory also shows that the same spin excitation that acts like a bosonic glue to hold the electron pairs together also mediates scattering of electrons in the strange-metal phase responsible for the linear in temperature resistivity in low temperatures.

PACS numbers: 74.25.Fy, 74.25.Nf, 74.20.Mn, 74.72.-h

I. INTRODUCTION

The parent compound of cuprate superconductors is identified as a Mott insulator¹, in which the absence of the electronic conduction is due to the strong electron correlation. Superconductivity then emerges when charge carriers are doped into this Mott insulator², therefore the physical properties of cuprate superconductors mainly depend on the extent of doping^{3–10}, and the regimes have been classified into the underdoped, optimally doped, and overdoped, respectively. At the temperature above the superconducting (SC) transition temperature T_c , the electron is in a normal-state. Although the same strong electron correlation that leads to the Mott insulating state persists into the doped regime, the normal-state retains a metallic character².

In the underdoped regime, the normal-state is dominated by a pseudogap. This pseudogap state is characterized by a substantial suppression of the density of the low-energy excitations^{3–6}. However, the resistivity in the pseudogap phase is quadratic in temperature (T-quadratic)^{7–13}, as would be expected from the standard Landau Fermi-liquid theory^{14–16}. On the other hand, in the optimally doped and overdoped regimes, the normal-state is characterized by a number of the anomalous low-temperature properties^{7–10} in the sense that they do not fit in with the standard Landau-Fermi liquid theory^{14–16}. This is why in the optimally doped and overdoped regimes, the phase above T_c is so-called as *the strange-metal phase*⁷. In particular, in the early experimental measurements^{17–19}, it was observed that the variation of the resistivity near the optimal doping is linear with temperature¹⁹, extending to low temperatures of a few kelvin and extrapolating to zero resistivity at zero temperature. This remarkable behaviour of the linear in temperature (T-linear) resistivity is in a striking contrast to the behaviour in conventional metals^{14–16}, where the

low-temperature resistivity follows one of several simple power laws, and if the electron-electron scattering dominates, then the resistivity decreases quadratically as the temperature decreases to zero. In the latter, this low-temperature T-linear resistivity was detected experimentally in a wide doping range of the overdoped regime^{20–26}. In particular, the suppression of superconductivity with a magnetic field reveals that the low-temperature T-linear resistivity persists down essentially to the zero temperature limit²⁷. Recently, the systematic experimental observations in the heavily overdoped regime yielded the low-temperature T-linear resistivity all the way up to the edge of the SC dome^{25–28}. After intensive investigations over more than three decades, it has now become clear that the long-standing low-temperature T-linear resistivity^{17–28} is a generic feature in the strange-metal phase of overdoped cuprate superconductors. In this case, a key question posed by these experimental observations is raised: is there a common bosonic excitation that is responsible for pairing the electrons also dominantly scatters the electrons in the strange-metal phase responsible for the low-temperature T-linear resistivity?

Although the low-temperature T-linear resistivity in the strange-metal phase of overdoped cuprate superconductors is well established by now^{17–28}, its origin remains the subject of the active research and debate. Theoretically, several scenarios have been proposed for the origin of the T-linear resistivity^{29–41}. In particular, in the marginal Fermi-liquid phenomenology^{29–31}, a single T-linear scattering rate is introduced responsible for the T-linear resistivity. Moreover, it has been postulated that the T-linear behaviour can be attributed to the strongly interacting critical state anchored at a quantum critical point (QCP) occurring at doping of about 0.20 where a phase transition is tuned to zero temperature^{31–33}. With the close relation to the physics of QCP, the T-linear resistivity has been interpreted in terms of the Planckian

dissipation^{34–38} in which the relaxation-time achieves a putative universal minimum value, irrespective of the underlying mechanisms. On the other hand, it has been argued that the elastic umklapp scattering processes, which directly transfer momentum between the electron sea and the underlying square lattice, lead to the T-linear resistivity in the strange-metal phase^{39,40}. More specifically, it has been shown recently that the resistance arises from the electron umklapp scattering mediated by a critical bosonic mode⁴¹, where the resistivity is characterized by a highly anisotropic scattering rate. This highly anisotropic scattering rate is T-linear near the umklapp point and becomes T-quadratic as one moves away from the umklapp point, which therefore leads to a T-linear resistivity in the low-temperature region and T-quadratic resistivity in the far-lower-temperature region⁴¹. These studies^{39–41} and many others^{42–44} therefore indicate that the electron umklapp scattering dominates the momentum-relaxation mechanism of the electrical transport. However, up to now, the origin of the low-temperature T-linear resistivity has not been discussed starting from a microscopic theory, and no explicit calculations of the doping dependence of the low-temperature T-linear resistivity has been made so far. Superconductivity with the highest T_c emerges directly as an instability of the strange-metal phase, and it thus has long been recognized that the understanding of the essential physics of the strange-metal phase is crucial for the understanding of the mystery of the unconventional superconductivity.

In the recent works within the framework of the kinetic-energy-driven superconductivity, we have studied the low-energy electronic structure of cuprate superconductors both in the SC-state^{45–47} and the strange-metal phase⁴⁸, where the electron normal self-energy in the particle-hole channel and electron anomalous self-energy in the particle-particle channel are generated by the coupling of the electrons with the spin excitations. In particular, the electrons are renormalized by the electron normal self-energy, and then all the exotic features of the low-energy electronic structure arise from this renormalization of the electrons^{45–48}. In this paper, we start from this low-energy electronic structure in the strange-metal phase of overdoped cuprate superconductors⁴⁸ to study the nature of the doping dependence of the low-temperature resistivity, where the momentum dependence of the transport scattering rate is arisen from the electron umklapp scattering mediated by the same spin excitation, and is employed to calculate the resistivity in terms of the Boltzmann equation. Our results show that the momentum dependence of the transport scattering rate presents a similar behavior of the single-particle scattering rate, and is largest at around the antinodes and smallest at around the tips of the Fermi arcs, indicating that the resistivity is mainly dominated by the antinodal and nodal umklapp scattering. In particular, a very low temperature T_{scale} scales with Δ_p^2 , where Δ_p is the minimal umklapp vector at the antinode. In the

low-temperature region ($T > T_{\text{scale}}$), the transport scattering rate is T-linear with the coefficient that decreases with the increase of doping. However, in the far-lower-temperature region ($T < T_{\text{scale}}$), the transport scattering rate is instead T-quadratic. This T-linear behaviour of the transport scattering rate in the low-temperature region and the T-quadratic behaviour in the far-lower-temperature region in turn generate respectively the T-linear resistivity in the low-temperature region and the T-quadratic resistivity in the far-lower-temperature region. Our results therefore indicate that the same spin excitation that is responsible for pairing the electrons also mediates the electron umklapp scattering in the strange-metal phase responsible for the low-temperature T-linear resistivity.

The rest of this paper is organized as follows. In Section II, we begin by a short summary of the unconventional features of the low-energy electronic structure due to the coupling of the electrons with the spin excitations, and then within the framework of the Boltzmann transport theory, we formulate the essential aspects of the electron umklapp scattering between a circular electron Fermi surface (EFS) and its umklapp partner mediated by the same spin excitation for deriving the resistivity. In Section III, the Boltzmann equation is employed to study the doping dependence of the low-temperature resistivity, where we show that both the strengths of the nodal and antinodal umklapp scattering decrease with the decrease of temperature. Finally, we give a summary and discussion in Section IV. In the Appendix A, we present the details of the derivation of the electron-electron collision term in the Boltzmann equation. In the Appendix B, we present the details for the estimate of the energy scale in the transport scattering rate at the umklapp point.

II. THEORY

A. t - J model in the fermion-spin representation

The crystal structure of cuprate superconductors is characterized by the square-lattice copper-oxide layers^{1–6}, which are sometimes considered to contain all the essential physics^{49–53}. Immediately after the discovery of superconductivity in cuprate superconductors, it was suggested that the fundamental properties of the doped copper-oxide layer are properly accounted by the square-lattice t - J model⁴⁹,

$$H = - \sum_{ll'\sigma} t_{ll'} C_{l\sigma}^\dagger C_{l'\sigma} + \mu \sum_{l\sigma} C_{l\sigma}^\dagger C_{l\sigma} + J \sum_{\langle ll' \rangle} \mathbf{S}_l \cdot \mathbf{S}_{l'}, \quad (1)$$

acting on the restricted Hilbert-space with no double electron occupancy $\sum_{\sigma} C_{l\sigma}^\dagger C_{l\sigma} \leq 1$, where the operator $C_{l\sigma}^\dagger$ ($C_{l\sigma}$) denotes the creation (annihilation) operator of an electron on site l with spin σ , \mathbf{S}_l is the spin operator of the electron with its components S_l^x , S_l^y , and S_l^z , and μ is the chemical potential. In this paper, the hopping of the constrained electrons $t_{ll'}$ is restricted to the

nearest-neighbor (NN) sites $\hat{\eta}$ with the hopping amplitude $t_{l\eta} = t$ and next NN sites $\hat{\tau}$ with the hopping amplitude $t_{l\tau} = -t'$. The summation $\langle ll' \rangle$ indicates a sum over the NN pairs, while the summation ll' is taken over all the NN and next NN pairs. Throughout this paper, we choose the parameters as $t/J = 2.5$ and $t'/t = 0.3$ as in the previous discussions⁴⁸. The magnitude of J and the lattice constant of the square lattice are the energy and length units, respectively. However, when necessary to compare with the experimental data, we set $J = 1000$ K.

The essence of the strongly correlated physics is reflected in the on-site local constraint of no double electron occupancy⁵⁰⁻⁵⁴. To avoid the double electron occupancy, we employ the fermion-spin transformation for the parametrization of the constrained electron operators $C_{l\uparrow}$ and $C_{l\downarrow}$ as^{55,56},

$$C_{l\uparrow} = h_{l\uparrow}^\dagger S_l^-, \quad C_{l\downarrow} = h_{l\downarrow}^\dagger S_l^+, \quad (2)$$

respectively, where the spin operator S_l keeps track of the spin degree of freedom of the constrained electron, while the spinful fermion operator $h_{l\sigma} = e^{-i\Phi_{l\sigma}} h_l$ keeps track of the charge degree of freedom of the constrained electron together with some effects of spin configuration rearrangements due to the presence of the doped hole itself (charge carrier). The advantages of this fermion-spin approach (2) can be summarized as: (i) the on-site local constraint of no double occupancy is satisfied in actual analyses; (ii) the charge carrier or spin *itself* is $U(1)$ gauge invariant^{55,56}, and then the collective mode for the spin is real and can be interpreted as the spin excitation responsible for the dynamical spin response, while the electron quasiparticle as a result of the charge-spin recombination of a charge carrier and a localized spin is not affected by the statistical $U(1)$ gauge fluctuation^{55,56}, and is responsible for the electronic-state properties. This is why the fermion-spin approach (2) is an efficient calculation scheme which can provide a good description of the anomalous properties of cuprate superconductors^{55,56}.

In this fermion-spin representation (2), the original t - J model (1) can be rewritten explicitly as,

$$H = \sum_{ll'\sigma} t_{ll'} (h_{l'\uparrow}^\dagger h_{l\uparrow} S_l^+ S_{l'}^- + h_{l'\downarrow}^\dagger h_{l\downarrow} S_l^- S_{l'}^+) - \mu_h \sum_{l\sigma} h_{l\sigma}^\dagger h_{l\sigma} + J_{\text{eff}} \sum_{\langle ll' \rangle} \mathbf{S}_l \cdot \mathbf{S}_{l'}, \quad (3)$$

where $S_l^- = S_l^x - iS_l^y$ and $S_l^+ = S_l^x + iS_l^y$ are the spin-lowering and spin-raising operators for the spin $S = 1/2$, respectively, $J_{\text{eff}} = (1 - \delta)^2 J$, $\delta = \langle h_{l\sigma}^\dagger h_{l\sigma} \rangle = \langle h_l^\dagger h_l \rangle$ is the charge-carrier doping concentration, and μ_h is the charge-carrier chemical potential. As a natural consequence, the kinetic-energy term in the t - J model (1) has been transferred as the coupling between charge and spin degrees of freedom of the constrained electron, which reflects a basic fact that even the kinetic energy term in the t - J model (1) has the strong Coulombic contribution due to the restriction of no double electron occupancy at an

any given site, and therefore governs the unconventional features of cuprate superconductors.

B. Coupling of electrons to the strongly dispersive spin excitation

Starting from the t - J model (3) in the fermion-spin representation, we⁵⁶⁻⁵⁹ have developed the kinetic-energy-driven superconductivity, where the charge-carrier attractive interaction comes from the strong coupling between charge and spin degrees of freedom of the constrained electron in the kinetic energy of the t - J model (3), and induces the d-wave charge-carrier pairing state, while the d-wave electron pairs originated from the d-wave charge-carrier pairs are due to the charge-spin recombination⁵⁹, and their condensation reveals the d-wave SC-state. In a similar to other distinct mechanisms for the spin-fluctuation driven pairing⁶⁰⁻⁶³, the kinetic-energy-driven SC mechanism is purely electronic without phonon, since the bosonic glue is identified into an electron pairing mechanism not involving the phonon, the external degree of freedom, but the internal spin degree of freedom of the constrained electron itself, indicating that the strong electron correlation favors superconductivity. Moreover, the kinetic-energy-driven SC-state is controlled by both the SC gap and single-particle coherence, which leads to that the doping dependence of T_c exhibits a dome-like shape with the underdoped and overdoped regimes on each side of the optimal doping, where T_c reaches its maximum⁵⁶⁻⁵⁹. In the kinetic-energy-driven superconductivity, the self-consistent equations⁵⁹ that are satisfied by the single-particle diagonal and off-diagonal propagators in the SC-state are obtained in terms of the Eliashberg formalism⁶⁴, and when the SC gap parameter $\bar{\Delta} = 0$, these self-consistent equations in the SC-state are reduced in the normal-state as⁴⁸,

$$G(\mathbf{k}, \omega) = G^{(0)}(\mathbf{k}, \omega) + G^{(0)}(\mathbf{k}, \omega) \Sigma_{\text{ph}}(\mathbf{k}, \omega) G(\mathbf{k}, \omega), \quad (4)$$

where $G^{(0)}(\mathbf{k}, \omega)$ is the single-particle (diagonal) propagator of the t - J model (1) in the tight-binding approximation, and has been derived as $G^{(0)-1}(\mathbf{k}, \omega) = \omega - \varepsilon_{\mathbf{k}}$. In this case, the single-particle propagator $G(\mathbf{k}, \omega)$ in Eq. (4) can be expressed explicitly as,

$$G(\mathbf{k}, \omega) = \frac{1}{\omega - \varepsilon_{\mathbf{k}} - \Sigma_{\text{ph}}(\mathbf{k}, \omega)}, \quad (5)$$

where $\varepsilon_{\mathbf{k}} = -4t\gamma_{\mathbf{k}} + 4t'\gamma'_{\mathbf{k}} + \mu$ is the electron energy dispersion in the tight-binding approximation, with $\gamma_{\mathbf{k}} = (\cos k_x + \cos k_y)/2$ and $\gamma'_{\mathbf{k}} = \cos k_x \cos k_y$, while the electron normal self-energy $\Sigma_{\text{ph}}(\mathbf{k}, \omega)$ sketched in Fig. 1 has been derived as⁴⁸,

$$\Sigma_{\text{ph}}(\mathbf{k}, \omega) = -4 \int_{-\infty}^{\infty} \frac{d\omega'}{2\pi} \int_{-\infty}^{\infty} \frac{d\omega''}{2\pi} \frac{n_{\text{B}}(\omega'') + n_{\text{F}}(\omega')}{\omega'' - \omega' + \omega} \times \frac{t^2}{N} \sum_{\mathbf{p}} \text{Im}G(\mathbf{p} + \mathbf{k}, \omega') \text{Im}P^{(0)}(\mathbf{k}, \mathbf{p}, \omega''), \quad (6)$$

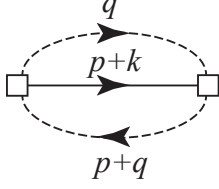


FIG. 1. The skeletal diagram for the electron normal self-energy for scattering electrons from the strongly dispersive spin excitations. The solid-line represents the electron propagator G , and the dashed-line depicts the spin propagator $D^{(0)}$, while \square describes the bare vertex function Λ .

where N is the number of lattice sites, $n_B(\omega)$ and $n_F(\omega)$ are the boson and fermion distribution functions, respectively, $\text{Im}P^{(0)}(\mathbf{k}, \mathbf{p}, \omega)$ is the imaginary part of $P^{(0)}(\mathbf{k}, \mathbf{p}, \omega)$, while $P^{(0)}(\mathbf{k}, \mathbf{p}, \omega)$ is so-called as the effective spin propagator, which describes the nature of the

spin excitation, and can be expressed as,

$$P^{(0)}(\mathbf{k}, \mathbf{p}, \omega) = \frac{1}{N} \sum_{\mathbf{q}} \Lambda_{\mathbf{p}+\mathbf{q}+\mathbf{k}}^2 \Pi(\mathbf{p}, \mathbf{q}, \omega), \quad (7)$$

with the bare vertex function $\Lambda_{\mathbf{k}} = 4\gamma_{\mathbf{k}} - 4(t'/t)\gamma'_{\mathbf{k}}$ and the spin bubble $\Pi(\mathbf{p}, \mathbf{q}, \omega)$ is a convolution of two spin propagators, and has been evaluated as⁴⁸,

$$\Pi(\mathbf{p}, \mathbf{q}, ip_m) = \frac{1}{\beta} \sum_{iq_m} D^{(0)}(\mathbf{q}, iq_m) D^{(0)}(\mathbf{q} + \mathbf{p}, iq_m + ip_m), \quad (8)$$

where p_m and q_m are the bosonic Matsubara frequencies, while the spin propagator $D^{(0)}(\mathbf{k}, \omega)$ in the mean-field (MF) level has been derived as,

$$D^{(0)}(\mathbf{k}, \omega) = \frac{B_{\mathbf{k}}}{\omega^2 - \omega_{\mathbf{k}}^2}, \quad (9)$$

with the MF spin excitation energy dispersion $\omega_{\mathbf{k}}$ and the weight function of the spin excitation spectrum $B_{\mathbf{k}}$ that have been obtained explicitly as⁵⁶,

$$\omega_{\mathbf{k}}^2 = \alpha \lambda_1^2 \left[\frac{1}{2} \epsilon \chi_1 (A_{11} - \gamma_{\mathbf{k}}) (\epsilon - \gamma_{\mathbf{k}}) + \chi_1^z (A_{12} - \epsilon \gamma_{\mathbf{k}}) (1 - \epsilon \gamma_{\mathbf{k}}) \right] + \alpha \lambda_2^2 \left[\left(\chi_2^z \gamma'_{\mathbf{k}} - \frac{3}{8} \chi_2 \right) \gamma'_{\mathbf{k}} + A_{13} \right] \\ + \alpha \lambda_1 \lambda_2 \left[\chi_1^z (1 - \epsilon \gamma_{\mathbf{k}}) \gamma'_{\mathbf{k}} + \frac{1}{2} (\chi_1 \gamma'_{\mathbf{k}} - C_3) (\epsilon - \gamma_{\mathbf{k}}) + \gamma'_{\mathbf{k}} (C_3^z - \epsilon \chi_2^z \gamma_{\mathbf{k}}) - \frac{1}{2} \epsilon (C_3 - \chi_2 \gamma_{\mathbf{k}}) \right], \quad (10a)$$

$$B_{\mathbf{k}} = \lambda_1 [2\chi_1^z (\epsilon \gamma_{\mathbf{k}} - 1) + \chi_1 (\gamma_{\mathbf{k}} - \epsilon)] - \lambda_2 (2\chi_2^z \gamma'_{\mathbf{k}} - \chi_2), \quad (10b)$$

where $\epsilon = 1 + 2t\phi_1/J_{\text{eff}}$, $\lambda_1 = 8J_{\text{eff}}$, $\lambda_2 = 16\phi_2 t'$, the charge-carrier's particle-hole parameters $\phi_1 = \langle h_{l\sigma}^\dagger h_{l+\hat{\eta}\sigma} \rangle$ and $\phi_2 = \langle h_{l\sigma}^\dagger h_{l+\hat{\tau}\sigma} \rangle$, $A_{11} = [(1 - \alpha)/8 - \alpha\chi_1^z/2 + \alpha C_1]/(\alpha\chi_1)$, $A_{12} = [(1 - \alpha)/16 - \alpha\epsilon\chi_1/8 + \alpha C_1^z]/(\alpha\chi_1^z)$, $A_{13} = [(1 - \alpha)/(8\alpha) - \chi_2^z/2 + C_2]/2$, the spin correlation functions $\chi_1 = \langle S_l^+ S_{l+\hat{\eta}}^- \rangle$, $\chi_2 = \langle S_l^+ S_{l+\hat{\tau}}^- \rangle$, $\chi_1^z = \langle S_l^z S_{l+\hat{\eta}}^z \rangle$, $\chi_2^z = \langle S_l^z S_{l+\hat{\tau}}^z \rangle$, $C_1 = (1/16) \sum_{\hat{\eta}, \hat{\eta}'} \langle S_{l+\hat{\eta}}^+ S_{l+\hat{\eta}'}^- \rangle$, $C_1^z = (1/16) \sum_{\hat{\eta}, \hat{\eta}'} \langle S_{l+\hat{\eta}}^z S_{l+\hat{\eta}'}^z \rangle$, $C_2 = (1/16) \sum_{\hat{\tau}, \hat{\tau}'} \langle S_{l+\hat{\tau}}^+ S_{l+\hat{\tau}'}^- \rangle$, $C_3 = (1/4) \sum_{\hat{\tau}} \langle S_{l+\hat{\tau}}^+ S_{l+\hat{\tau}}^- \rangle$, and $C_3^z = (1/4) \sum_{\hat{\tau}} \langle S_{l+\hat{\tau}}^z S_{l+\hat{\tau}}^z \rangle$. In order to satisfy the sum rule of the correlation function $\langle S_l^+ S_l^- \rangle = 1/2$ in the case without an antiferromagnetic long-range order (AFLRO), the important decoupling parameter α has been introduced in the calculation⁵⁶, which can be regarded as the vertex correction. At the half-filling, the degree of freedom is local spin only, where $\epsilon = 1$, $\lambda_2 = 0$, $\chi_1^z = \chi_1/2$, $C_1^z = C_1/2$, and then the above MF spin excitation energy dispersion $\omega_{\mathbf{k}}$ and the weight function $B_{\mathbf{k}}$ in Eq. (10) are reduced as, $\omega_{\mathbf{k}} = \lambda_1 \sqrt{\alpha |\chi_1| (1 - \gamma_{\mathbf{k}}^2)}$ and $B_{\mathbf{k}} = -2\lambda_1 \chi_1 (1 - \gamma_{\mathbf{k}})$, respectively. This spin

excitation energy dispersion at the half-filling is the standard spin-wave dispersion. However, in the doped regime without an AFLRO, although the expression form of the MF spin excitation energy dispersion $\omega_{\mathbf{k}}$ in Eq. (10a) is rather complicated, the essential feature of the spin-wave nature is the same as that in the case of the half-filling⁵⁶.

Substituting the above MF spin propagator (9) into Eq. (8), the spin bubble $\Pi(\mathbf{p}, \mathbf{q}, \omega)$ can be derived as,

$$\Pi(\mathbf{p}, \mathbf{q}, \omega) = -\frac{\bar{W}_{\mathbf{p}\mathbf{q}}^{(1)}}{\omega^2 - [\omega_{\mathbf{p}\mathbf{q}}^{(1)}]^2} + \frac{\bar{W}_{\mathbf{p}\mathbf{q}}^{(2)}}{\omega^2 - [\omega_{\mathbf{p}\mathbf{q}}^{(2)}]^2}, \quad (11)$$

and then the effective spin propagator $P^{(0)}(\mathbf{k}, \mathbf{p}, \omega)$ in Eq. (7) is obtained directly from the above spin bubble (11), where the spin excitation energy dispersions $\omega_{\mathbf{p}\mathbf{q}}^{(1)} = \omega_{\mathbf{q}+\mathbf{p}} + \omega_{\mathbf{q}}$ and $\omega_{\mathbf{p}\mathbf{q}}^{(2)} = \omega_{\mathbf{q}+\mathbf{p}} - \omega_{\mathbf{q}}$, and the weight functions of the effective spin excitation spectrum,

$$\bar{W}_{\mathbf{p}\mathbf{q}}^{(1)} = \frac{B_{\mathbf{q}} B_{\mathbf{q}+\mathbf{p}}}{2\omega_{\mathbf{q}} \omega_{\mathbf{q}+\mathbf{p}}} \omega_{\mathbf{p}\mathbf{q}}^{(1)} [n_B(\omega_{\mathbf{q}+\mathbf{p}}) + n_B(\omega_{\mathbf{q}}) + 1], \quad (12)$$

$$\bar{W}_{\mathbf{p}\mathbf{q}}^{(2)} = \frac{B_{\mathbf{q}}B_{\mathbf{q}+\mathbf{p}}}{2\omega_{\mathbf{q}}\omega_{\mathbf{q}+\mathbf{p}}}\omega_{\mathbf{p}\mathbf{q}}^{(2)}[n_{\mathbf{B}}(\omega_{\mathbf{q}+\mathbf{p}}) - n_{\mathbf{B}}(\omega_{\mathbf{q}})]. \quad (13)$$

It thus shows that the essential behaviors of the spin excitation energy dispersions $\omega_{\mathbf{p}\mathbf{q}}^{(1)}$ and $\omega_{\mathbf{p}\mathbf{q}}^{(2)}$ are mainly governed by the essential behaviors of the MF spin excitation energy dispersion $\omega_{\mathbf{k}}$ in Eq. (10a).

With the above effective spin propagator (7), the electron normal self-energy $\Sigma_{\text{ph}}(\mathbf{k}, \omega)$ in Eq. (6) has been obtained explicitly in Ref. 48. In particular, it should be emphasized that all the order parameters and chemical potential μ in the calculation of $\Sigma_{\text{ph}}(\mathbf{k}, \omega)$ have been determined by the self-consistent calculation^{56–59}. In this sense, our calculation for $\Sigma_{\text{ph}}(\mathbf{k}, \omega)$ is controllable without using adjustable parameters. Moreover, the sharp peaks visible for low-temperature in $\Sigma_{\text{ph}}(\mathbf{k}, \omega)$ and $P^{(0)}(\mathbf{k}, \mathbf{p}, \omega)$ are actually a δ -function, broadened by a small damping used in the numerical calculation for a finite lattice^{65,66}. The calculation in this paper for $\Sigma_{\text{ph}}(\mathbf{k}, \omega)$ and $P^{(0)}(\mathbf{k}, \mathbf{p}, \omega)$ is performed numerically on a 160×160 lattice in momentum space, with the infinitesimal $i0_+ \rightarrow i\Gamma$ replaced by a small damping $\Gamma = 0.05J$.

C. Electron Fermi surface

The single-particle spectrum function $A(\mathbf{k}, \omega)$ now can be obtained directly from the above single-particle propagator (5) as,

$$A(\mathbf{k}, \omega) = -2\text{Im}G(\mathbf{k}, \omega) = \frac{2\Gamma_{\mathbf{k}}(\omega)}{[\omega - \bar{E}_{\mathbf{k}}(\omega)]^2 + \Gamma_{\mathbf{k}}^2(\omega)}, \quad (14)$$

with the corresponding single-particle scattering rate $\Gamma_{\mathbf{k}}(\omega)$ and renormalized band structure $\bar{E}_{\mathbf{k}}(\omega)$,

$$\Gamma_{\mathbf{k}}(\omega) = |\text{Im}\Sigma_{\text{ph}}(\mathbf{k}, \omega)|, \quad (15a)$$

$$\bar{E}_{\mathbf{k}}(\omega) = \varepsilon_{\mathbf{k}} + \text{Re}\Sigma_{\text{ph}}(\mathbf{k}, \omega), \quad (15b)$$

where $\text{Re}\Sigma_{\text{ph}}(\mathbf{k}, \omega)$ and $\text{Im}\Sigma_{\text{ph}}(\mathbf{k}, \omega)$ are the real and imaginary parts of the electron normal self-energy $\Sigma_{\text{ph}}(\mathbf{k}, \omega)$, respectively.

The shape of EFS has deep consequences for the low-energy electronic properties^{3–7}, and has been also central to addressing electrical transport^{8–10}. In the previous studies⁴⁸, the topology of EFS in the strange-metal phase of cuprate superconductors has been discussed in terms of the intensity map of the single-particle spectral function (14) at zero energy $\omega = 0$, where it has been shown that (i) the EFS continuous contour is determined by the poles of the single-particle propagator (5) at zero energy, i.e., $\varepsilon_{\mathbf{k}} + \text{Re}\Sigma_{\text{ph}}(\mathbf{k}, 0) = \bar{\varepsilon}_{\mathbf{k}} = 0$, with the renormalized electron energy dispersion $\bar{\varepsilon}_{\mathbf{k}} = Z_{\text{F}}\varepsilon_{\mathbf{k}}$ and the single-particle coherent weight $Z_{\text{F}}^{-1} = 1 - \text{Re}\Sigma_{\text{pho}}(\mathbf{k}, 0)|_{\mathbf{k}=[\pi, 0]}$, where $\Sigma_{\text{pho}}(\mathbf{k}, \omega)$ is the antisymmetric part of the electron normal self-energy $\Sigma_{\text{ph}}(\mathbf{k}, \omega)$; (ii) however, a strong redistribution of the spectral weight on EFS is induced by the highly anisotropic momentum dependence of the single-particle scattering rate $\Gamma_{\mathbf{k}}(\omega)$. For a convenience

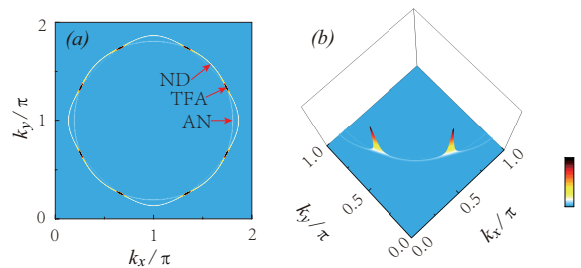


FIG. 2. (Color online) (a) The map of the electron Fermi surface and (b) the surface plot of the electron spectral function for zero energy $\omega = 0$ at $\delta = 0.18$ with $T = 0.002J$, where the Brillouin zone center has been shifted by $[\pi, \pi]$, and AN, TFA, and ND denote the antinode, tip of the Fermi arc, and node, respectively.

in the following discussions of the electrical transport, we plot (a) the EFS map and (b) the direct surface plot of the single-particle spectral function $A(\mathbf{k}, \omega)$ for zero energy $\omega = 0$ at doping $\delta = 0.18$ with temperature $T = 0.002J$ in Fig. 2, where the Brillouin zone (BZ) center has been shifted by $[\pi, \pi]$, and AN, TFA, and ND indicate the antinode, tip of the Fermi arc, and node, respectively. The most noteworthy in Fig. 2 are the following: (i) the spectral weight at around the antinodal region is suppressed strongly, reflecting a basic fact that EFS at around the antinodal region can not be observed experimentally^{67–79}; (ii) the spectral weight at around the nodal region is suppressed modestly, leading to the formation of the disconnected Fermi arcs^{67–79}, where the Fermi arc increases its length as a function of doping^{73–79}, and then it evolves into a continuous contour in momentum space near the end of the SC dome; (iii) however, almost all the spectral weight on the Fermi arcs is assembled at around the tips of the Fermi arcs^{67–79}. In other words, the electrons at around the tips of the Fermi arcs have a largest density of states, and then the low-energy electronic properties are largely governed by these electrons at around the tips of the Fermi arcs. In particular, it has been observed experimentally that these characteristic features shown in Fig. 2 in the zero energy case can persist into the case for a finite binding-energy even in the optimally and overdoped regimes^{79,80}. More importantly, the suppression of the spectral weight at around the antinodal and nodal regions can affect the electrical transport in two ways⁹: through the reduction of the number of current-carrying states, and secondly, through the reduction in the density of electron excitations at around the antinodal and nodal regions.

In our previous discussions⁴⁸, it has been shown that the origin of the spectral redistribution to form the Fermi arcs can be attributed to the highly anisotropic momentum dependence of the single-particle scattering rate $\Gamma(\theta)$, where $\Gamma(\theta)$ is defined as $\Gamma(\theta) = \Gamma_{\mathbf{k}_{\text{F}}(\theta)}(0)$, and θ is the Fermi angle. To see this highly anisotropic $\Gamma(\theta)$ in momentum space more clearly, we plot the angular dependence of $\Gamma(\theta)$ along EFS from the antinode to the

node at $\delta = 0.18$ with $T = 0.05J$ in Fig. 3, where the actual minimum of $\Gamma(\theta)$ does not appear at around the nodal region, but resides exactly at around the tip of the Fermi arc. However, the maximal $\Gamma(\theta)$ appears at around the antinodal region, and then $\Gamma(\theta)$ decreases when the Fermi angle is moved away from the antinode. In particular, $\Gamma(\theta)$ at around the nodal region is smaller than that around the antinodal region. This angular dependence of $\Gamma(\theta)$ therefore leads to the spectral redistribution to form the Fermi arcs with almost all the spectral weight inhabited at around the tips of the Fermi arcs.

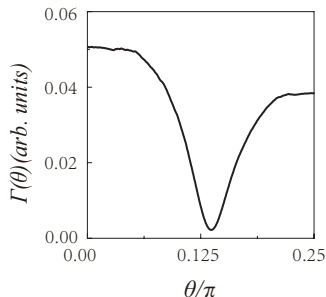


FIG. 3. The single-particle scattering rate $\Gamma(\theta)$ as a function of Fermi angle θ at $\delta = 0.18$ with $T = 0.05J$ for $\omega = 0$.

With the help of the above single-particle spectrum function (14), we have also studied the renormalization of the electrons in the strange-metal phase of overdoped cuprate superconductors⁴⁸, including the EFS instability driven charge order together with the related octet scattering model^{76,77,79–84}, the complicated line-shape in the energy distribution curve^{85–89}, and the kink in the electron dispersion^{90–95}, and the obtained results are well consistent with the corresponding experimental observations. In particular, it should be emphasized that the similar results^{96–99} have been also obtained based on the phenomenological spin-fermion approach^{62,99}, where the coupling of a spin excitation to electron quasiparticles leads to the emergence of the spectral dip in the energy distribution curve and the kink in the quasiparticle dispersion^{96–99}. These results^{48,96–99} therefore show that the same spin excitation that is responsible for pairing the electrons also dominantly scatters the electrons in the strange-metal phase responsible for the low-energy electronic structure.

D. Boltzmann equation

Although the magnitude of the single-particle scattering rate $\Gamma(\theta)$ shown in Fig. 3 at a given Fermi angle is different from that of the corresponding transport scattering rate³¹, both the scattering rates may have a similar behaviour of the angular dependence. In this sense, the result of the angular dependence of $\Gamma(\theta)$ in Fig. 3 also indicates that the important electron scattering responsible for the resistivity is mainly concentrated at around the

antinodes and nodes. For the discussions of the transport properties, it is needed to determine how the momentum distribution relaxes in the vicinity of these antinodes and nodes. However, in the strange-metal phase of overdoped cuprate superconductors, there are no well-defined quasiparticle excitations^{7–10}. In this case, the momentum distribution relaxes in the system can be discussed in terms of the memory-matrix transport formalism^{100–105} or by solving the Boltzmann equation with the input of the scattering processes^{15,16}. The memory-matrix transport formalism^{100–105} has a crucial advantage of not relying on the existence of well-defined quasiparticle excitations. In particular, this memory-matrix transport approach has been employed to study the electrical transport in the strange-metal phase of different strongly correlated models^{100–105}, and the obtained results are consistent with the rather severe set by experiments. On the other hand, in the Boltzmann transport theory^{15,16}, it is crucial to assume that either the quasiparticle excitations are well-defined or that the effective interaction between electrons via various bosonic modes can be treated within the Eliashberg approach⁶⁴ as shown by Prange and Kadanoff¹⁰⁶ for an electron-phonon system. In this paper, we study the electrical transport in the strange-metal phase of overdoped cuprate superconductors by solving the Boltzmann equation with the input of the scattering process, since the electron interaction mediated by the spin excitation in the framework of the kinetic-energy-driven superconductivity^{56–59} is treated within the Eliashberg approach⁶⁴ as we have mentioned in subsection II B. In the Boltzmann transport theory^{15,16}, the essential behaviour of the electrons is depicted by the distribution function $f(\mathbf{r}, \mathbf{k}, t)$. In the following discussions, we focus on the dc conductivity in the homogeneous system only, where the position and time dependence in the distribution function are absent, and then the distribution function satisfies the following Boltzmann equation^{15,16},

$$\frac{\partial \mathbf{k}}{\partial t} \cdot \nabla_{\mathbf{k}} f(\mathbf{k}) = \left(\frac{df}{dt} \right)_{\text{collisions}} \quad (16)$$

where the right-hand side is the time rate of change due to the electron-electron collision, while the factor $\partial \mathbf{k} / \partial t$ is equivalent to an acceleration, which is equal to the forces on the electrons as,

$$\frac{\partial \mathbf{k}}{\partial t} = -e\mathbf{E}, \quad (17)$$

with the charge e , where for a convenience in the following discussions, the magnetic field has been dropped, i.e., $\mathbf{H} = 0$, while only an electric field \mathbf{E} is applied to the system. In this case, we substitute Eq. (17) into Eq. (16), and rewrite the Boltzmann equation (16) as,

$$e\mathbf{E} \cdot \nabla_{\mathbf{k}} f(\mathbf{k}) + \left(\frac{df}{dt} \right)_{\text{collisions}} = 0. \quad (18)$$

Following the discussions in Refs. 106 and 41, we now introduce the linear perturbation from the equilibrium in

terms of the distribution function as,

$$f(\mathbf{k}) = n_F(\bar{\varepsilon}_{\mathbf{k}}) - \frac{dn_F(\bar{\varepsilon}_{\mathbf{k}})}{d\bar{\varepsilon}_{\mathbf{k}}} \tilde{\Phi}(\mathbf{k}), \quad (19)$$

where $\tilde{\Phi}(\mathbf{k})$ has been interpreted as a local shift of the chemical potential at a given patch of EFS^{41,106}, and satisfies an antisymmetric relation $\tilde{\Phi}(-\mathbf{k}) = -\tilde{\Phi}(\mathbf{k})$. With the help of the above distribution function (19), the Boltzmann equation (18) can be linearized with the result that can be expressed explicitly as,

$$e\mathbf{v}_{\mathbf{k}} \cdot \mathbf{E} \frac{\partial n_F(\bar{\varepsilon}_{\mathbf{k}})}{\partial \bar{\varepsilon}_{\mathbf{k}}} = - \left(\frac{df}{dt} \right)_{\text{collisions}} = I_{e-e}, \quad (20)$$

where $\mathbf{v}_{\mathbf{k}} = \nabla_{\mathbf{k}} \bar{\varepsilon}_{\mathbf{k}}$ is the electron velocity and I_{e-e} is the electron-electron collision term.

E. Electron umklapp scattering

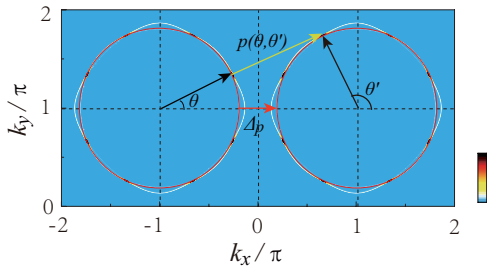


FIG. 4. (Color online) Illustration of the umklapp scattering process⁴¹ in which an electron on a circular electron Fermi surface (left) is scattered by its partner on the umklapp electron Fermi surface (right), where the intensity map of the electron Fermi surface is the same as shown in Fig. 2a, while the perfect circle (red) is the circle with the radius k_F^{TFA} , where k_F^{TFA} is the Fermi wave vector of the tips of the Fermi arcs. An electron on the electron Fermi surface (left) parametrized by the Fermi angle θ is scattered to a point parametrized by the Fermi angle θ' on the umklapp electron Fermi surface (right) by the spin excitation carrying momentum $p(\theta, \theta')$. The minimal umklapp vector is Δ_p at the antinode (the Fermi angle $\theta = 0$). This physical picture is repeated for the other three umklapp electron Fermi surfaces that are closest to the original electron Fermi surface.

For evaluating the electron-electron collision in the Boltzmann equation (20), the mechanism of the momentum relaxation needs to be introduced^{15,16}. After in-

tensive investigations over more than three decades, although the mechanism of the momentum relaxation for the T-linear resistivity still remains controversial, the electron umklapp scattering is believed to be at the heart of the striking behaviour of the electrical transport in the strange-metal phase of overdoped cuprate superconductors³⁹⁻⁴⁴. In this paper, we adopt the electron umklapp scattering as the mechanism of the momentum relaxation, and then study the electrical transport in the strange-metal phase of overdoped cuprate superconductors. For a convenience in the following discussions, the schematic picture for the electron umklapp scattering process⁴¹ is illustrated in Fig. 4, where an electron on a circular EFS (left) is scattered by its partner on the umklapp EFS (right). In Fig. 4, the intensity map of EFS is the same as in Fig. 2a, while the perfect circle (red) is the circle with the radius k_F^{TFA} , where k_F^{TFA} is the Fermi wave vector of the tips of the Fermi arcs. This perfect circle EFS (red) connects all eight tips of the Fermi arcs, and thus shows that almost all the spectral weight of the electron excitation spectrum is accommodated on this circle EFS. It should be emphasized that in the present case, the electron umklapp scattering is mediated by the same spin excitation as in the case of the electron scattering for the renormalization of the electrons in subsection II B. To understand the umklapp scattering mechanism in the present case more clearly, the skeletal diagram of this umklapp scattering mechanism in energy and momentum space is drawn in Fig. 5.

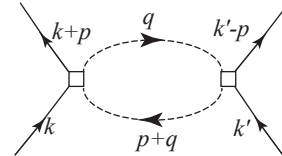


FIG. 5. The skeletal diagram of the umklapp scattering process for scattering electrons from the spin excitation. The solid-line represents the electron propagator G , and the dashed-line depicts the spin propagator $D^{(0)}$, while \square describes the bare vertex function Λ .

In the recently pioneering work⁴¹, a model of the electrons scattered by a critical bosonic mode with the umklapp scattering being the dominant momentum relaxation mechanism has been studied, where the umklapp scattering process is described as an electron-electron scattering via the exchange of the critical boson propagator, rather than the scattering between electrons via the emission and absorption of bosons. Following their discussions⁴¹, the electron-electron collision I_{e-e} in Eq. (20) originated from the electron umklapp scattering shown in Fig. 5 can be evaluated as,

$$\begin{aligned}
I_{e-e} = & \frac{1}{N^2} \sum_{\mathbf{k}', \mathbf{p}} \frac{2}{T} |P(\mathbf{k}, \mathbf{p}, \mathbf{k}', \bar{\epsilon}_{\mathbf{k}} - \bar{\epsilon}_{\mathbf{k}+\mathbf{p}+\mathbf{G}})|^2 \{ \tilde{\Phi}(\mathbf{k}) + \tilde{\Phi}(\mathbf{k}') - \tilde{\Phi}(\mathbf{k} + \mathbf{p} + \mathbf{G}) - \tilde{\Phi}(\mathbf{k}' - \mathbf{p}) \} \\
& \times n_{\text{F}}(\bar{\epsilon}_{\mathbf{k}}) n_{\text{F}}(\bar{\epsilon}_{\mathbf{k}'}) [1 - n_{\text{F}}(\bar{\epsilon}_{\mathbf{k}+\mathbf{p}+\mathbf{G}})] [1 - n_{\text{F}}(\bar{\epsilon}_{\mathbf{k}'-\mathbf{p}})] \delta(\bar{\epsilon}_{\mathbf{k}} + \bar{\epsilon}_{\mathbf{k}'} - \bar{\epsilon}_{\mathbf{k}+\mathbf{p}+\mathbf{G}} - \bar{\epsilon}_{\mathbf{k}'-\mathbf{p}}), \quad (21)
\end{aligned}$$

which therefore leads to the appearance of the electrical resistance^{15,16}, where \mathbf{G} indicates a set of reciprocal lattice vectors, and the umklapp scattering process in Eq. (21) is described as an electron-electron scattering via the exchange of the effective spin propagator $P(\mathbf{k}, \mathbf{p}, \mathbf{k}', \omega)$, rather than the scattering between electrons via the emission and absorption of the spin excitation, while the effective spin propagator $P(\mathbf{k}, \mathbf{p}, \mathbf{k}', \omega)$ is obtained directly from Fig. 5 as,

$$P(\mathbf{k}, \mathbf{p}, \mathbf{k}', \omega) = \frac{1}{N} \sum_{\mathbf{q}} \Lambda_{\mathbf{p}+\mathbf{q}+\mathbf{k}} \Lambda_{\mathbf{q}+\mathbf{k}'} \Pi(\mathbf{p}, \mathbf{q}, \omega). \quad (22)$$

The reason of the electron-electron scattering via the exchange of the effective spin propagator in the present case is the same as in the case discussed in Ref. 41. For the normal scattering ($\mathbf{G} = 0$), the conservation of the total momentum in Eq. (21) is satisfied straightforwardly⁴¹, since the distribution in the case of the normal scattering will rapidly equilibrate to a fermion distribution function with a shifted overall momentum $\tilde{\Phi}(\mathbf{k}) \propto \mathbf{k} \cdot \mathbf{E}$, which leads to that its contribution to the integral of the electron-electron collision in Eq. (21) is exactly zero. However, if we consider the scattering between electrons via the emission and absorption of the spin excitation, we would have to keep track of the extra shifted boson distribution function as well, which introduces more complications⁴¹. Moreover, it has been shown that the vanishing of the normal scattering in the electron-electron collision (21) is more general⁴¹. This is following a basic fact that in order to stay on EFS and conserve the total momentum and energy, the momentum of the normal scattering partner \mathbf{k}' must equal to either $\mathbf{k} + \mathbf{p}$ or $-\mathbf{k}$. In the former case, the last two terms in $\{\dots\}$ in Eq. (21) cancel the first two terms. However, in the latter case, since the antisymmetric relation $\tilde{\Phi}(-\mathbf{k}) = -\tilde{\Phi}(\mathbf{k})$, the first two terms in $\{\dots\}$ in Eq. (21) cancel, while the same cancellation is valid for the last two terms corresponding to the outgoing pair $\mathbf{k} + \mathbf{p}$ and $\mathbf{k}' - \mathbf{p}$. These results therefore indicate that the contribution from the normal scattering to the integral of the electron-electron collision (21) is negligible⁴¹.

In the usual case^{15,16}, the derivation of the Boltzmann equation starting from the nonequilibrium electron propagator involves integrating over energy ω . However, the electrons at the bottom of the band (then the deep inside EFS) can not be thermally excited, and as a matter of the principle, all the low-temperature conduction processes in the strange-metals should involve only states at around EFS³⁶. In particular, in the early discussions¹⁰⁶, it has been realized to pick a patch of EFS specified by $k(\theta)$ with the range $\theta \in [0, 2\pi]$, which defines a contour

along EFS parametrized by the direction θ of the Fermi momentum vector and integrate the perpendicular momentum and hence over $\bar{\epsilon}_{\mathbf{k}}$ instead. This is a formula expressed entirely in terms of the EFS property. Furthermore, this method has been employed to study the low-temperature T-linear resistivity due to the umklapp scattering from a critical bosonic mode⁴¹. In the present case of the electron umklapp scattering mediated by the spin excitation, an electron on EFS parametrized by the Fermi angle θ is scattered to a point parametrized by the Fermi angle θ' on the umklapp EFS by the spin excitation carrying momentum $\mathbf{p}(\theta, \theta')$ as shown in Fig. 4. In this case, the usual distribution function $f(\mathbf{k})$ can be replaced as $f[k(\theta)]$. However, in the usual formulation, the vector \mathbf{k} is decomposed into $k(\theta)$ and the momentum in the perpendicular direction^{41,106}, which is then represented by $\bar{\epsilon}_{\mathbf{k}}$. From this EFS parametrization, the standard Boltzmann equation (20) now can be expressed simply, where the component of the momentum \mathbf{k} perpendicular to EFS is replaced by $\bar{\epsilon}_{\mathbf{k}}/v_{\mathbf{k}}$ and $\bar{\epsilon}_{\mathbf{k}}$ in turn is replaced by ω . After a straightforward calculation [see Appendix A], the above electron-electron collision I_{e-e} in Eq. (21) can be derived explicitly, and then the Boltzmann equation (20) can be obtained as,

$$e\mathbf{v}_{\text{F}}(\theta) \cdot \mathbf{E} = -2 \int \frac{d\theta'}{2\pi} \zeta(\theta') F(\theta, \theta') [\Phi(\theta) - \Phi(\theta')], \quad (23)$$

where $\Phi(\theta)$ is defined as $\tilde{\Phi}[k(\theta)]$ and satisfies an antisymmetric relation⁴¹ $\Phi(\theta) = -\Phi(\theta + \pi)$, $\mathbf{v}_{\text{F}}(\theta)$ is the Fermi velocity at the Fermi angle θ , and $\zeta(\theta') = k_{\text{F}}^2/[4\pi^2 v_{\text{F}}^3]$ is the density of states factor at angle θ' with the Fermi wave vector k_{F} and Fermi velocity v_{F} , while the coefficient of $\Phi(\theta)$ in the first term of the right-hand side of Eq. (23),

$$\gamma(\theta) = 2 \int \frac{d\theta'}{2\pi} \zeta(\theta') F(\theta, \theta'), \quad (24)$$

is defined as the scattering out rate⁴¹ from the state of $k(\theta)$, which also is so-called as *the angular dependence of the transport scattering rate*, while the kernel function $F(\theta, \theta')$ depends on the Fermi angles θ and θ' in terms of the magnitude of the momentum transfer $\mathbf{p}(\theta, \theta')$, i.e., $F(\theta, \theta')$ connects the points θ and θ' on the umklapp EFS as shown in Fig. 4, and is given by,

$$\begin{aligned}
F(\theta, \theta') = & \frac{1}{T} \int \frac{d\omega}{2\pi} \frac{\omega^2}{\mathbf{p}(\theta, \theta')} |\bar{P}[\mathbf{k}(\theta), \mathbf{p}(\theta, \theta'), \omega]|^2 \\
& \times n_{\text{B}}(\omega) [1 + n_{\text{B}}(\omega)], \quad (25)
\end{aligned}$$

where the reduced effective spin propagator $\bar{P}[\mathbf{k}(\theta), \mathbf{p}(\theta, \theta'), \omega]$ has been given in Appendix A.

This kernel function $F(\theta, \theta')$ can be also called as the probability weight or the strength of the umklapp scattering.

III. LOW-TEMPERATURE T-LINEAR RESISTIVITY

The dc conductivity then is evaluated in a standard way by the momentum (then the Fermi angle θ) integral of the umklapp scattering process on EFS, where the current density is given by^{15,16},

$$\mathbf{J} = -en_0 \frac{1}{N} \sum_{\mathbf{k}} \mathbf{v}_{\mathbf{k}} f(\mathbf{k}), \quad (26)$$

with the momentum relaxation that is generated by the action of the electric field on the mobile electrons³⁶ at around EFS with the density n_0 . Substituting the distribution function $f(\mathbf{k})$ in Eq. (19) into the above current density equation (26) and performing the radial integration, the current density now can be obtained as,

$$\begin{aligned} \mathbf{J} &= en_0 \frac{1}{N} \sum_{\mathbf{k}} \mathbf{v}_{\mathbf{k}} \frac{dn_{\mathbf{F}}(\bar{\epsilon}_{\mathbf{k}})}{d\bar{\epsilon}_{\mathbf{k}}} \tilde{\Phi}(\mathbf{k}) \\ &= -en_0 \frac{k_{\mathbf{F}}}{v_{\mathbf{F}}} \int \frac{d\theta}{(2\pi)^2} \mathbf{v}_{\mathbf{F}}(\theta) \Phi(\theta). \end{aligned} \quad (27)$$

For deriving the dc conductivity, we need to obtain the local shift of the chemical potential $\Phi(\theta)$. The spectral weight of $\text{Im}P(\mathbf{k}_{\mathbf{F}}, \mathbf{p} - \mathbf{k}_{\mathbf{F}}, \mathbf{k}'_{\mathbf{F}}, \omega)$ in Eq. (21) achieves its maximal value at around the antinodal region [see Fig. 12 in Appendix A], where the scattering probability for two electrons is largest. In other words, the main contribution to the kernel function $F(\theta, \theta')$ comes from such umklapp scattering process in which the electron at around the antinodal region of the circular EFS (left) shown in Fig. 4 is scattered by its partner at around the antinodal region of the umklapp circular EFS (right), where the Fermi angle θ' is almost identical with the Fermi angle $\pi - \theta$, and then according to the antisymmetric relation satisfied by $\Phi(\theta)$, the following relation,

$$\Phi(\theta') = \Phi(\pi - \theta) = -\Phi(\theta), \quad (28)$$

is valid. In this relaxation-time approximation, the local shift of the chemical potential $\Phi(\theta)$ can be derived straightforwardly from Eqs. (23) and (24) as⁴¹,

$$\Phi(\theta) = -\frac{ev_{\mathbf{F}} \cos(\theta) E_{\hat{x}}}{2\gamma(\theta)}, \quad (29)$$

where the electric field \mathbf{E} has been chosen along the \hat{x} -axis. Substituting the above result of $\Phi(\theta)$ into Eq. (27), the dc conductivity therefore is obtained explicitly as,

$$\sigma_{\text{dc}}(T) = \frac{1}{2} e^2 n_0 k_{\mathbf{F}} v_{\mathbf{F}} \int \frac{d\theta}{(2\pi)^2} \cos^2(\theta) \frac{1}{\gamma(\theta)}, \quad (30)$$

and then the resistivity is obtained directly from the above dc conductivity as,

$$\rho(T) = \frac{1}{\sigma_{\text{dc}}(T)}. \quad (31)$$

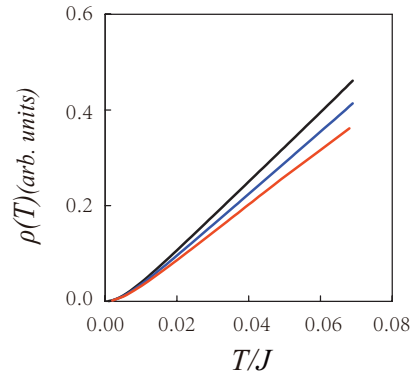


FIG. 6. (Color online) The resistivity as a function of temperature at $\delta = 0.15$ (black-line), $\delta = 0.18$ (blue-line), and $\delta = 0.24$ (red-line).

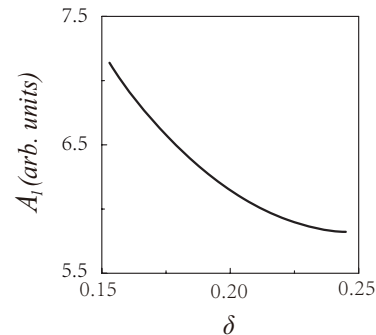


FIG. 7. T-linear resistivity coefficient as a function of doping.

Now we are ready to discuss the striking features of the electrical transport in the strange-metal phase of overdoped cuprate superconductors. We have made a series of calculations for the resistivity $\rho(T)$ in Eq. (31) at different doping levels, and the results of the resistivity $\rho(T)$ as a function of temperature at the doping concentrations $\delta = 0.15$ (black-line), $\delta = 0.18$ (blue-line), and $\delta = 0.24$ (red-line) are plotted in Fig. 6. Apparently, the experimental results of the doping dependence of the low-temperature resistivity¹⁷⁻²⁸ are qualitatively reproduced, where the highly unconventional features can be summarized as: (i) the resistivity $\rho(T)$ as a function of temperature is a perfect straight line down to the temperature $T \sim 0.015J = 15\text{K}$; (ii) the low-temperature T-linear resistivity extends over a wide doping range in the overdoped regime, where the T-linear resistivity coefficient A_1 (then the strength of the T-linear resistivity) decreases with the increase of doping. To see

this doping dependence of the T-linear resistivity coefficient more clearly, we plot A_1 versus doping δ in Fig. 7, where A_1 *increases* monotonically as the doping concentration is reduced in the overdoped regime, this tendency of the doping dependence is in qualitative agreement with the experimental observations on overdoped cuprate superconductors^{25,27}; (iii) however, the resistivity deviates from the pure T-linearity in the far-lower-temperature region $T < 0.015J = 15K$, while our numerical fit indicates that in this far-lower-temperature region, the resistivity decreases quadratically as the temperature decreases. The results in Fig. 6 therefore also indicate that the same spin excitation that acts like a bosonic glue to hold the electron pairs together responsible for superconductivity^{56–59} also dominates the electron umklapp scattering responsible for the low-temperature T-linear resistivity in the strange-metal phase.

Finally, it should be emphasized that the local shift of the chemical potential $\Phi(\theta)$ can be also evaluated directly by the numerical solution of the Boltzmann equation (23) together with an additional electron-impurity collision without making the relaxation-time approximation⁴¹, where the Fermi angle θ' variable in Eq. (23) can be discretized, and then the integral-differential equation (23) is converted into the matrix equation. The accurate result of $\Phi(\theta)$ is obtained in terms of the numerical calculation of the inverse of this matrix. In this case, we have also performed a numerical calculation $\Phi(\theta)$ [then $\rho(T)$], and the results show that although the resistivity saturates to a constant $\rho_0(T)$ induced by the impurity, the qualitative behaviour of the resistivity is the same as that obtained in the above relaxation-time approximation except for the subtle difference of slopes, which is also qualitatively consistent with the results obtained from the electron umklapp scattering mediated by a critical bosonic mode⁴¹.

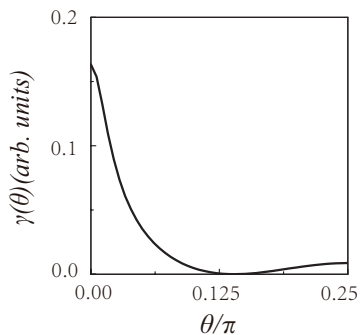


FIG. 8. The transport scattering rate $\gamma(\theta)$ as a function of Fermi angle θ at $\delta = 0.18$ with $T = 0.05J$.

From the dc conductivity in Eq. (30) [then the resistivity in Eq. (31)], it thus shows that the low-temperature T-linear resistivity in the strange-metal phase can be attributed to the angle and temperature dependence of the transport scattering rate $\gamma(\theta, T)$ in Eq. (24). To see this point more clearly, we first plot $\gamma(\theta)$ as a function

of Fermi angle θ at $\delta = 0.18$ with $T = 0.05J$ in Fig. 8. In a comparison with the corresponding angular dependence of the single-particle scattering rate $\Gamma(\theta)$ in Fig. 3, it shows that although the magnitude of $\gamma(\theta)$ at any given Fermi angle is less than that of $\Gamma(\theta)$ at the corresponding Fermi angle, the global behaviour of the angular dependence of $\gamma(\theta)$ is similar to that of $\Gamma(\theta)$, where $\gamma(\theta)$ is largest at around the antinodal region, and smallest at around the tips of the Fermi arcs, which is also consistent with the strong momentum dependence of the effective spin propagator $P(\mathbf{k}, \mathbf{p} - \mathbf{k}, \mathbf{k}', \omega)$ shown in Fig. 12 in Appendix A. In other words, both the transport scattering rate $\gamma(\theta)$ and single-particle scattering rate $\Gamma(\theta)$ as a function of Fermi angle presents a similar behavior of the effective spin propagator $P(\mathbf{k}, \mathbf{p} - \mathbf{k}, \mathbf{k}', \omega)$. The result in Fig. 8 therefore also shows that the resistivity is mainly dominated by the transport scattering rate at both the antinodal and nodal regions.

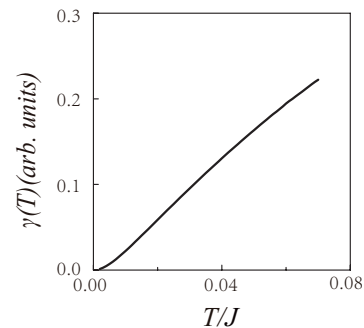


FIG. 9. The transport scattering rate $\gamma(T)$ at the antinode as a function of temperature for $\delta = 0.18$.

On the other hand, for an any given Fermi angle θ , $\gamma(\theta, T)$ varies strongly with temperature. To see this temperature dependence of $\gamma(\theta, T)$ more clearly, we plot $\gamma(T)$ as a function of temperature for $\delta = 0.18$ at the antinode in Fig. 9. It is surprising that $\gamma(T)$ is entirely T-linear in the low-temperature region $T > 0.015J = 15K$, where it decreases linearly with temperature as the temperature decreases to $T \sim 0.015J = 15K$, while this transport scattering rate $\gamma(T)$ is instead T-quadratic in the far-lower-temperature region $T < 0.015J = 15K$. Moreover, although $\gamma(\theta, T)$ is highly anisotropic in momentum-space, this low-temperature T-linear $\gamma(\theta, T)$ occurs at an any given Fermi angle θ (then for all directions), in agreement with the experimental observations²⁸. In a comparison with the corresponding results of the temperature dependence of the resistivity shown in Fig. 6, we therefore find that the T-linear behaviour of $\gamma(T)$ together with the temperature region and the T-quadratic behaviour of $\gamma(T)$ together with the temperature region are respectively the same as the corresponding behaviours and regions in the resistivity $\rho(T)$, which shows clearly that the T-linear resistivity with the temperature region and the T-quadratic resistivity with the temperature region are governed respectively by the

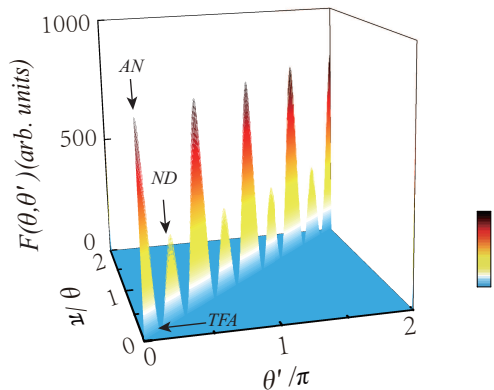


FIG. 10. (Color online) The surface plot of the kernel function $F(\theta, \theta')$ at $\delta = 0.18$ with $T = 0.05J$, where AN, TFA, and ND denote the antinode, tip of the Fermi arc, and node, respectively.

T-linear transport scattering rate with the temperature region and T-quadratic transport scattering rate with the temperature region.

For a further understanding of the nature of the transport scattering rate $\gamma(\theta, T)$, we discuss the temperature dependence of the kernel function $F(\theta, \theta')$ in Eq. (25), since the temperature dependence of $\gamma(\theta, T)$ in Eq. (24) is mainly determined by the temperature dependence of $F(\theta, \theta')$. In Fig. 10, we plot the surface plot of $F(\theta, \theta')$ at $\delta = 0.18$ with $T = 0.05J$, where the probability weight of the electron umklapp scattering has been separated clearly into three characteristic regions: (i) the antinodal region, where a particularly large fraction of the probability weight is located, leading to that $\gamma(\theta)$ is largest at around the antinodal region; (ii) the nodal region, where a small amount of the probability weight is inhabited, leading to that the magnitude of $\gamma(\theta)$ at around the nodal region is much smaller than that at around the antinodal region; (iii) the region at around the tips of the Fermi arcs, where the strength of the umklapp scattering is anomalously small, leading to the appearance of the weakest scattering at around the tips of the Fermi arcs. The characteristic feature of the tips of the Fermi arcs is that both the real and imaginary parts of the electron normal self-energy have the anomalously small values⁴⁸, indicating that the interaction (then the scattering) between electrons at around the tips of the Fermi arcs is particularly weak. In other words, although the electron density of states is largest at around the tips of the Fermi arcs, the electron scattering at around the tips of the Fermi arcs is quite weak, and then the electrons at around the tips of the Fermi arcs move more freely than those at other parts of EFS. The above result in Fig. 10 indicates that the electron umklapp scattering is concentrated at around the antinodes and nodes, and therefore is well consistent with the result of the angular dependence of $\gamma(\theta, T)$ shown in Fig. 8. How-

ever, the strengths of the antinodal and nodal umklapp scattering are temperature dependent, which induces a competition between the antinodal and nodal umklapp scattering, and can be well understood in terms of the ratio of the strength of the nodal umklapp scattering to the strength of the antinodal umklapp scattering,

$$R_F(T) = \frac{F(\theta_{ND}, \theta'_{ND}, T)}{F(\theta_{AN}, \theta'_{AN}, T)}.$$

However, as we have mentioned in subsection II B, the

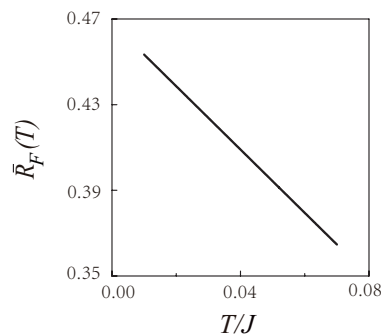


FIG. 11. The ratio of the strength of the nodal umklapp scattering to the strength of the antinodal umklapp scattering as a function of temperature for $\delta = 0.18$.

calculation in this paper is performed numerically for a finite lattice, which leads to that the weight of the δ -function type peak in $F(\theta, \theta')$ at the antinode (node) spreads on the extremely small area $\{\theta_{AN}\}$ $\{\theta_{ND}\}$ around the antinode (node) as shown in Fig. 10. In particular, the summation of these spread weights around this extremely small area $\{\theta_{AN}\}$ $\{\theta_{ND}\}$ is less affected by the calculation for a finite lattice. In this case, a more appropriate ratio can be obtained as,

$$\bar{R}_F(T) = \frac{\bar{F}_{ND}(T)}{\bar{F}_{AN}(T)}, \quad (32)$$

for the reduction of the size effect in the finite-lattice calculation, where $\bar{F}_{AN}(T)$ and $\bar{F}_{ND}(T)$ are given by,

$$\begin{aligned} \bar{F}_{AN}(T) &= \frac{1}{2\pi} \sum_{\substack{\theta_{AN} \in \{\theta_{AN}\} \\ \theta'_{AN} \in \{\theta'_{AN}\}}} F(\theta, \theta', T), \\ \bar{F}_{ND}(T) &= \frac{1}{2\pi} \sum_{\substack{\theta_{ND} \in \{\theta_{ND}\} \\ \theta'_{ND} \in \{\theta'_{ND}\}}} F(\theta, \theta', T), \end{aligned}$$

with the summation $\theta_{AN} \in \{\theta_{AN}\}$ $\{\theta'_{AN} \in \{\theta'_{AN}\}\}$ that is restricted to the extremely small area $\{\theta_{AN}\}$ $\{\theta_{ND}\}$ around the antinode (node). In this case, we have carried out a series of calculations for the ratio $\bar{R}_F(T)$ at different doping levels, and the result of $\bar{R}_F(T)$ as a function of temperature at $\delta = 0.18$ is plotted in Fig. 11, where $\bar{R}_F(T)$ decreases monotonically with the increase of temperature. In other words, although both the strengths

of the nodal and antinodal umklapp scattering decrease with the decrease of temperature, the decrease of the strength of the nodal umklapp scattering is slower than that of the antinodal umklapp scattering.

We now turn to show why the transport scattering rate $\gamma(T)$ [then the resistivity $\rho(T)$] exhibits a crossover from the T-linear behaviour in the low-temperature region into T-quadratic behaviour in the far-lower-temperature region? The expression form of the kernel function $F(\theta, \theta')$ in Eq. (25) indicates that $F(\theta, \theta')$ is proportional to the effective spin propagator $P(\mathbf{k}, \mathbf{p}, \mathbf{k}', \omega)$. For a convenience in the following discussions, the effective spin propagator $P(\mathbf{k}, \mathbf{p}, \mathbf{k}', \omega)$ in Eq. (22) can be rewritten as,

$$P(\mathbf{k}, \mathbf{p}, \mathbf{k}', \omega) = -\frac{1}{N} \sum_{\mathbf{q}, j} (-1)^{j+1} \frac{\varpi_j(\mathbf{k}, \mathbf{p}, \mathbf{k}', \mathbf{q})}{\omega^2 - [\omega_{\mathbf{p}\mathbf{q}}^{(j)}]^2}, \quad (33)$$

$$\begin{aligned} F(\theta, \theta') &= \frac{1}{T} \frac{1}{N^2} \sum_{\mathbf{q}, \mathbf{q}', j, j'} (-1)^{j+j'} P \int_{-\infty}^{\infty} \frac{d\omega}{2\pi} \frac{\omega^2}{p(\theta, \theta')} \frac{e^{\beta\omega}}{[e^{\beta\omega} - 1]^2} \frac{\varpi_j(\theta, \theta', \mathbf{q})}{\omega^2 - [\omega_{\theta\theta'}^{(j)}(\mathbf{q})]^2} \frac{\varpi_{j'}(\theta, \theta', \mathbf{q}')}{\omega^2 - [\omega_{\theta\theta'}^{(j')}(\mathbf{q}')]^2} \\ &= \frac{1}{N^2} \sum_{\mathbf{q}, \mathbf{q}', j, j'} (-1)^{j+j'} \frac{\varpi_j(\theta, \theta', \mathbf{q}) \varpi_{j'}(\theta, \theta', \mathbf{q}')}{2\pi p(\theta, \theta')} \frac{1}{T^2} i2\pi I[C_j(\theta, \theta', \mathbf{q}), C_{j'}(\theta, \theta', \mathbf{q}')], \end{aligned} \quad (35)$$

with $\varpi_j(\theta, \theta', \mathbf{q}) = \varpi_j[k(\theta), p(\theta, \theta'), \mathbf{k}'_{\mathbf{F}}, \mathbf{q}]$, $\varpi_{j'}(\theta, \theta', \mathbf{q}') = \varpi_{j'}[k(\theta), p(\theta, \theta'), \mathbf{k}'_{\mathbf{F}}, \mathbf{q}']$, $\omega_{\theta\theta'}^{(j)}(\mathbf{q}) = \omega_{p(\theta, \theta'), \mathbf{q}}^{(j)}$, $\omega_{\theta\theta'}^{(j')}(\mathbf{q}') = \omega_{p(\theta, \theta'), \mathbf{q}'}^{(j')}$, and the function,

$$I_{jj'}(\theta, \theta', \mathbf{q}, \mathbf{q}') = P \int_{-\infty}^{\infty} \frac{dx}{i2\pi} \frac{e^x}{(e^x - 1)^2} \frac{x^2}{[x^2 - C_j^2(\theta, \theta', \mathbf{q})][x^2 - C_{j'}^2(\theta, \theta', \mathbf{q}')]}, \quad (36)$$

where $C_j(\theta, \theta', \mathbf{q})$ and $C_{j'}(\theta, \theta', \mathbf{q}')$ are defined as $C_j(\theta, \theta', \mathbf{q}) = \omega_{\theta\theta'}^{(j)}(\mathbf{q})/T$ and $C_{j'}(\theta, \theta', \mathbf{q}') = \omega_{\theta\theta'}^{(j')}(\mathbf{q}')/T$, respectively. From the MF spin propagator in Eq. (9), the spin spectral function can be obtained directly as,

$$A_{\text{spin}}(\mathbf{k}) = \pi \frac{B_{\mathbf{k}}}{\omega_{\mathbf{k}}} [\delta(\omega - \omega_{\mathbf{k}}) - \delta(\omega + \omega_{\mathbf{k}})], \quad (37)$$

where the MF spin excitation energy spectrum $\omega_{\mathbf{k}}$ is an even function of momentum \mathbf{k} , and in particular, $\omega_{\mathbf{k}}|_{\mathbf{k}=\mathbf{k}_A}$ has an extremely small value⁵⁶ [$\omega_{\mathbf{k}_A} = 0.00205J \approx 2\text{K}$ at doping $\delta = 0.18$], where $\mathbf{k}_A = [\pm\pi, \pm\pi]$ is the antiferromagnetic wave vector, which therefore leads to that the spin excitations at around the \mathbf{k}_A point of BZ have the largest density of states, and then the spin response is mainly governed by these spin excitations. In this case, the effective spin excitation energy dispersions $\omega_{\mathbf{p}\mathbf{q}}^{(1)}$ and $\omega_{\mathbf{p}\mathbf{q}}^{(2)}$ in Eq. (11) can be expanded, and then can be expressed approximately as,

$$\omega_{\mathbf{p}\mathbf{q}}^{(1)} = \omega_{\mathbf{q}+\mathbf{p}} + \omega_{\mathbf{q}} \approx a(\mathbf{q})p^2 + 2\omega_{\mathbf{q}}, \quad (38a)$$

$$\omega_{\mathbf{p}\mathbf{q}}^{(2)} = \omega_{\mathbf{q}+\mathbf{p}} - \omega_{\mathbf{q}} \approx a(\mathbf{q})p^2, \quad (38b)$$

with $j = 1, 2$, the weight functions $\varpi_1(\mathbf{k}, \mathbf{p}, \mathbf{k}', \mathbf{q})$ and $\varpi_2(\mathbf{k}, \mathbf{p}, \mathbf{k}', \mathbf{q})$ that are given by,

$$\varpi_1(\mathbf{k}, \mathbf{p}, \mathbf{k}', \mathbf{q}) = \Lambda_{\mathbf{k}+\mathbf{p}+\mathbf{q}} \Lambda_{\mathbf{q}+\mathbf{k}'} \bar{W}_{\mathbf{p}\mathbf{q}}^{(1)}, \quad (34a)$$

$$\varpi_2(\mathbf{k}, \mathbf{p}, \mathbf{k}', \mathbf{q}) = \Lambda_{\mathbf{k}+\mathbf{p}+\mathbf{q}} \Lambda_{\mathbf{q}+\mathbf{k}'} \bar{W}_{\mathbf{p}\mathbf{q}}^{(2)}. \quad (34b)$$

Substituting above result in Eq. (33) into Eq. (25), the kernel function $F(\theta, \theta')$ can be rewritten as,

where $a(\mathbf{q}) = (d^2\omega_{\mathbf{q}}/d^2\mathbf{q})$. The results in Eq. (38) therefore indicate that the effective spin propagator $P(\mathbf{k}, \mathbf{p}, \mathbf{k}', \omega)$ in Eq. (33) is scaled by p^2 . However, due to this p^2 scaling in the effective spin propagator (33), the temperature scale when the electron umklapp scattering kicks in can be very low⁴¹, being proportional to Δ_p^2 , where Δ_p is the minimal umklapp vector at the antinode shown in Fig. 4. In other words, $\bar{a}\Delta_p^2$ is referred to as the temperature scale, i.e., $T_{\text{scale}} = \bar{a}\Delta_p^2$, where $\bar{a} = (1/N) \sum_{\mathbf{q}} a(\mathbf{q})$ is the average value, and is a constant at a given doping. Moreover, this temperature scale is obtained numerically as $T_{\text{scale}} = \bar{a}\Delta_p^2 = 0.01513J \approx 15\text{K}$ at doping $\delta = 0.18$, which is well consistent with the crossover temperature shown in Fig. 6. In this case, the function $I_{jj'}(\theta, \theta', \mathbf{q}, \mathbf{q}')$ in the above equation (36) can be derived respectively in three different temperature regions:

- (i) in the region for finite values of $C_j(\theta, \theta', \mathbf{q})$ and $C_{j'}(\theta, \theta', \mathbf{q}')$, the function $I_{jj'}(\theta, \theta', \mathbf{q}, \mathbf{q}')$ in Eq. (36) can be evaluated [see Appendix B] as,

$$I_{jj'}(\theta, \theta', \mathbf{q}, \mathbf{q}') = i \frac{1}{2[C_j^2(\theta, \theta', \mathbf{q}) - C_{j'}^2(\theta, \theta', \mathbf{q}')] } \left(\frac{C_j(\theta, \theta', \mathbf{q})e^{C_j(\theta, \theta', \mathbf{q})}}{[e^{C_j(\theta, \theta', \mathbf{q})} - 1]^2} - \frac{C_{j'}(\theta, \theta', \mathbf{q}')e^{C_{j'}(\theta, \theta', \mathbf{q}')}}{[e^{C_{j'}(\theta, \theta', \mathbf{q}')} - 1]^2} \right). \quad (39)$$

In particular, in the low-temperature region, which is corresponding to the case of $T > [T_{\text{scale}} + \omega_{\mathbf{k}_A}]$, the function $I_{jj'}(\theta, \theta', \mathbf{q}, \mathbf{q}')$ in the above equation (39) can be reduced as $I_{jj'}(\theta, \theta', \mathbf{q}, \mathbf{q}') \sim -iT^3/[4(\bar{a}\Delta_p^2)^3]$, and then kernel function in Eq. (35) in the low-temperature region is obtained explicitly as,

$$F(\theta, \theta') \approx \frac{1}{N^2} \sum_{\mathbf{q}, \mathbf{q}', jj'} (-1)^{j+j'} \frac{\varpi_j(\theta, \theta', \mathbf{q})\varpi_{j'}(\theta, \theta', \mathbf{q}')}{2p(\theta, \theta')} \frac{T}{\omega_{\theta\theta'}^{(j)}(\mathbf{q})\omega_{\theta\theta'}^{(j')}(\mathbf{q}')[\omega_{\theta\theta'}^{(j)}(\mathbf{q}) + \omega_{\theta\theta'}^{(j')}(\mathbf{q}')] } \propto T, \quad (40)$$

which leads to the transport scattering rate $\gamma(T) \propto T$ [then the resistivity $\rho(T) \propto T$] in the low-temperature region; (ii) on the other hand, in the far-lower-temperature region, which is corresponding to the case of $T < T_{\text{scale}}$, the function $I_{jj'}(\theta, \theta', \mathbf{q}, \mathbf{q}')$ in Eq. (36) can be derived straightforwardly as,

$$\begin{aligned} I_{jj'}(\theta, \theta', \mathbf{q}, \mathbf{q}') &= -i \frac{1}{2\pi C_j^2(\theta, \theta', \mathbf{q})C_{j'}^2(\theta, \theta', \mathbf{q}')} \int_0^\infty dx \frac{e^x}{(e^x - 1)^2} \frac{x^2}{[1 - x^2/C_j^2(\theta, \theta', \mathbf{q})][1 - x^2/C_{j'}^2(\theta, \theta', \mathbf{q}')] } \\ &= -i \frac{1}{2\pi C_j^2(\theta, \theta', \mathbf{q})C_{j'}^2(\theta, \theta', \mathbf{q}')} \int_0^\infty dx \frac{e^x x^2}{(e^x - 1)^2} \left[1 + \frac{x^2}{C_j^2(\theta, \theta', \mathbf{q})} + \left(\frac{x^2}{C_j^2(\theta, \theta', \mathbf{q})} \right)^2 + \dots \right] \\ &\times \left[1 + \frac{x^2}{C_{j'}^2(\theta, \theta', \mathbf{q}') } + \left(\frac{x^2}{C_{j'}^2(\theta, \theta', \mathbf{q}')} \right)^2 + \dots \right] \approx -i \frac{1}{2\pi C_j^2(\theta, \theta', \mathbf{q})C_{j'}^2(\theta, \theta', \mathbf{q}')} \int_0^\infty dx \frac{e^x x^2}{(e^x - 1)^2} \\ &= -i \frac{1}{6C_j^2(\theta, \theta', \mathbf{q})C_{j'}^2(\theta, \theta', \mathbf{q}')} = -i \frac{T^4}{6[\bar{a}\Delta_p^2]^2[\bar{a}\Delta_p^2 + \omega_{\mathbf{k}_A}]^2}, \end{aligned} \quad (41)$$

and then the kernel function in Eq. (35) can be obtained in the far-lower-temperature region as,

$$F(\theta, \theta') \approx \frac{1}{N^2} \sum_{\mathbf{q}, \mathbf{q}', jj'} (-1)^{j+j'} \frac{\varpi_j(\theta, \theta', \mathbf{q})\varpi_{j'}(\theta, \theta', \mathbf{q}')}{6p(\theta, \theta')} \frac{1}{T^2} \frac{T^4}{[\bar{a}\Delta_p^2]^2[\bar{a}\Delta_p^2 + \omega_{\mathbf{k}_A}]^2} \propto T^2, \quad (42)$$

which naturally gives rise to a T-quadratic behaviour of the transport scattering rate $\gamma(T) \propto T^2$ [then the resistivity $\rho(T) \propto T^2$] in the far-lower-temperature region; (iii) however, in the temperature region of $T_{\text{scale}} < T < T_{\text{scale}} + \omega_{\mathbf{k}_A}$, which is corresponding to the crossover region of the transport scattering rate. In this extremely narrow crossover region (from $\sim 15\text{K}$ to $\sim 17\text{K}$), the resistivity is neither T-linear nor T-quadratic, but is a nonlinear in temperature. The above results therefore explain why the resistivity has a crossover from the T-linear behaviour in the low-temperature region into the T-quadratic behaviour in the far-lower-temperature region. The above results also show that the effect of the umklapp scattering via the exchange of the effective spin propagator is not exponentially small at the low-temperature region as in the case of the electron-phonon coupling, but is power law down to the far-lower-temperature region as in the case of the coupling of the electrons with a critical bosonic mode⁴¹.

IV. SUMMARY AND DISCUSSION

Starting from the low-energy electronic structure of the strange-metal phase in overdoped cuprate superconductors, we have studied the nature of the low-temperature electrical transport, where the angular dependence of the transport scattering rate is arisen from the umklapp scattering between electrons by the exchange of the effective spin propagator, and is employed to evaluate the resistivity by making use of the Boltzmann equation. Our results show that although the magnitude of the transport scattering rate at an any given Fermi angle is smaller than the corresponding value of the single-particle scattering rate, the transport scattering rate presents a similar behavior of the single-particle scattering rate, where the transport scattering rate is largest at around the antinodal region and smallest at around the tips of the Fermi arcs, indicating that the resistivity is mainly dominated by the antinodal and nodal umklapp scattering. In particular, a very low temperature T_{scale} scales with Δ_p^2 , this leads to that in the low-temperature region ($T > T_{\text{scale}}$), the transport scattering rate is T-linear with the T-linear resistivity co-

efficient that decreases with the increase of doping. However, in the far-lower-temperature region ($T < T_{\text{scale}}$), the transport scattering rate is instead T-quadratic. This T-linear behaviour of the transport scattering rate in the low-temperature region and T-quadratic behaviour in the far-lower-temperature region in turn induces respectively the T-linear resistivity in the low-temperature region and T-quadratic resistivity in the far-lower-temperature region. Our theory also shows that the same spin excitation that acts like a bosonic glue to hold the electron pairs together responsible for the exceptionally high T_c also mediates the electron umklapp scattering in the strange-metal phase of overdoped cuprate superconductors responsible for the T-linear resistivity.

It should be emphasized that the effective spin propagator $P(\mathbf{k}, \mathbf{p}, \mathbf{k}', \omega)$ in Eq. (22) is obtained in the MF level^{48,56}, i.e., $P(\mathbf{k}, \mathbf{p}, \mathbf{k}', \omega)$ in Eq. (22) is obtained as a convolution of two MF spin propagators in Eq. (9). Thus the umklapp scattering between electrons in Eq. (21) by the exchange of this effective MF spin propagator is better suited for the discussions of the electrical transport in the strange-metal phase of overdoped cuprate superconductors as in case of the umklapp scattering between electron by the exchange of the phenomenologically critical bosonic mode⁴¹. This follows a basic fact that in the overdoped regime, the effect of the magnetic fluctuation becomes quite weak^{1,9,10,99}, and then the scattering between electrons by the exchange of the effective MF spin propagator can give a suitable description of the renormalization of the electrons^{45–48} and the related electrical transport discussed in this paper. However, in the underdoped regime, where the magnetic fluctuation is particularly strong^{1,9,10,99} and can be described in terms of the full spin propagator^{107–109}, where the spin self-energy is derived in terms of the charge-carrier bubble, and then the umklapp scattering between electrons

should be mediated by the exchange of the effective full spin propagator for a suitable discussion of the electrical transport in the underdoped cuprate superconductors. These and the related issues are under investigation now. The transport scattering mechanism developed in this paper for the understanding of the electrical transport in the strange-metal phase of overdoped cuprate superconductors can be also employed to study the electrical transport in other families of strange metals^{110,111} in the doped regime, where the magnetic fluctuation is rather weak. In particular, based on this transport scattering theory, we have also discussed the low-temperature T-linear resistivity of the electron-doped cuprate superconductors in the overdoped regime¹¹², where we show the common mechanism linking the electrical transport of both the hole- and electron-doped cuprate superconductors in the overdoped regime. These and the related works will be presented elsewhere.

ACKNOWLEDGEMENTS

The authors would like to thank Dr. Lin Zhao and Dr. Xiang Li for the helpful discussions. This work is supported by the National Key Research and Development Program of China under Grant No. 2021YFA1401803, and the National Natural Science Foundation of China under Grant Nos. 11974051, 12274036, and 12247116.

Appendix A: Derivation of electron-electron collision

The aim of this Appendix is to derive the electron-electron collision I_{e-e} in Eq. (23) of the main text. The electron-electron collision in Eq. (21) can be also rewritten as,

$$I_{e-e} = \frac{1}{N^2} \sum_{\mathbf{k}', \mathbf{p}} \frac{2}{T} |P(\mathbf{k}, \mathbf{p} - \mathbf{k}, \mathbf{k}', \bar{\epsilon}_{\mathbf{k}} - \bar{\epsilon}_{\mathbf{p}+\mathbf{G}})|^2 [\tilde{\Phi}(\mathbf{k}) + \tilde{\Phi}(\mathbf{k}') - \tilde{\Phi}(\mathbf{p} + \mathbf{G}) - \tilde{\Phi}(\mathbf{k}' + \mathbf{k} - \mathbf{p})] \\ \times n_{\text{F}}(\bar{\epsilon}_{\mathbf{k}}) n_{\text{F}}(\bar{\epsilon}_{\mathbf{k}'})[1 - n_{\text{F}}(\bar{\epsilon}_{\mathbf{p}+\mathbf{G}})][1 - n_{\text{F}}(\bar{\epsilon}_{\mathbf{k}'+\mathbf{k}-\mathbf{p}})] \delta(\bar{\epsilon}_{\mathbf{k}} + \bar{\epsilon}_{\mathbf{k}'} - \bar{\epsilon}_{\mathbf{p}+\mathbf{G}} - \bar{\epsilon}_{\mathbf{k}'+\mathbf{k}-\mathbf{p}}), \quad (\text{A1})$$

with the effective spin propagator $P(\mathbf{k}, \mathbf{p} - \mathbf{k}, \mathbf{k}', \omega)$ that can be expressed explicitly as,

$$P(\mathbf{k}, \mathbf{p} - \mathbf{k}, \mathbf{k}', \omega) = \frac{1}{N} \sum_{\mathbf{q}} \Lambda_{\mathbf{p}+\mathbf{q}} \Lambda_{\mathbf{q}+\mathbf{k}'} \Pi(\mathbf{p} - \mathbf{k}, \mathbf{q}, \omega) = \int_{-\infty}^{\infty} \frac{d\omega'}{\pi} \frac{\text{Im}P(\mathbf{k}, \mathbf{p} - \mathbf{k}, \mathbf{k}', \omega')}{\omega' - \omega}, \quad (\text{A2})$$

where the imaginary part of the effective spin propagator $\text{Im}P(\mathbf{k}, \mathbf{p} - \mathbf{k}, \mathbf{k}', \omega)$ is directly related to the effective spin spectral function, and is also defined as the scattering probability for two electrons. However, in our previous discussions¹¹³, we have shown that for given momentums \mathbf{k} and \mathbf{k}' , $\text{Im}P(\mathbf{k}, \mathbf{p} - \mathbf{k}, \mathbf{k}', \omega)$ exhibits a remarkable evolution with momentum \mathbf{p} and ω except for $\omega = 0$, where $\text{Im}P(\mathbf{k}, \mathbf{p} - \mathbf{k}, \mathbf{k}', 0) = 0$. To see this unusual

momentum \mathbf{p} dependence of $\text{Im}P(\mathbf{k}, \mathbf{p} - \mathbf{k}, \mathbf{k}', \omega)$ more clearly, we plot the intensity map of $\text{Im}P(\mathbf{k}, \mathbf{p} - \mathbf{k}, \mathbf{k}', \omega)$ along EFS $\mathbf{k} = \mathbf{k}' = \mathbf{k}_{\text{F}}$ in a $[p_x, p_y]$ plane at $\delta = 0.18$ for energy $\omega = -0.05J$ with $T = 0.002J$ in Fig. 12, where the spectral weight of $\text{Im}P(\mathbf{k}_{\text{F}}, \mathbf{p} - \mathbf{k}_{\text{F}}, \mathbf{k}'_{\text{F}}, \omega)$ along EFS $\mathbf{k} = \mathbf{k}' = \mathbf{k}_{\text{F}}$ converges on the corresponding EFS $\mathbf{p} = \mathbf{k}_{\text{F}}$, i.e., $\text{Im}P(\mathbf{k}_{\text{F}}, \mathbf{p} - \mathbf{k}_{\text{F}}, \mathbf{k}'_{\text{F}}, \omega) \neq 0$ for $\mathbf{p} = \mathbf{k}_{\text{F}}$, and otherwise $\text{Im}P(\mathbf{k}_{\text{F}}, \mathbf{p} - \mathbf{k}_{\text{F}}, \mathbf{k}'_{\text{F}}, \omega) = 0$. In

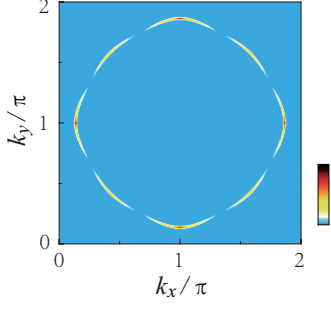


FIG. 12. (Color online) The intensity map of the imaginary part of the effective spin propagator $\text{Im}P(\mathbf{k}, \mathbf{p} - \mathbf{k}, \mathbf{k}', \omega)$ along $\mathbf{k} = \mathbf{k}' = \mathbf{k}_F$ in a $[p_x, p_y]$ plane at $\delta = 0.18$ for energy $\omega = -0.05J$ with $T = 0.002J$.

particular, the spectral weight of $\text{Im}P(\mathbf{k}_F, \mathbf{p} - \mathbf{k}_F, \mathbf{k}'_F, \omega)$ exhibits a largest value at around the antinodal region, however, the most striking feature is that the actual minimum of the spectral weight of $\text{Im}P(\mathbf{k}_F, \mathbf{p} - \mathbf{k}_F, \mathbf{k}'_F, \omega)$ does not appear at around the node, but locates exactly at the tips of the Fermi arcs. This special angular dependence of $\text{Im}P(\mathbf{k}_F, \mathbf{p} - \mathbf{k}_F, \mathbf{k}'_F, \omega)$ therefore induces an EFS reconstruction to form the Fermi arcs as shown in Fig. 2 with almost all the spectral weight of the electron excitation spectrum that resides at around the tips of the Fermi arcs.

The result shown in Fig. 12 therefore indicates that the main contribution in $P(\mathbf{k}, \mathbf{p} - \mathbf{k}, \mathbf{k}', \omega)$ comes from the part of the momentum $\mathbf{p} = \mathbf{k}$. In this case, the term $\Phi(\mathbf{k}') - \Phi(\mathbf{k}' + \mathbf{k} - \mathbf{p}) \sim 0$ in the right-hand side of Eq. (A1), and then $\delta(\bar{\epsilon}_{\mathbf{k}} + \bar{\epsilon}_{\mathbf{k}'} - \bar{\epsilon}_{\mathbf{p}+\mathbf{G}} - \bar{\epsilon}_{\mathbf{k}'+\mathbf{k}-\mathbf{p}})$ in the right-hand side of Eq. (A1) can be replaced by the integral identity as⁴¹,

$$\delta(\bar{\epsilon}_{\mathbf{k}} + \bar{\epsilon}_{\mathbf{k}'} - \bar{\epsilon}_{\mathbf{p}+\mathbf{G}} - \bar{\epsilon}_{\mathbf{k}'+\mathbf{k}-\mathbf{p}}) = \int_{-\infty}^{\infty} d\omega \delta(\bar{\epsilon}_{\mathbf{k}} - \bar{\epsilon}_{\mathbf{p}+\mathbf{G}} - \omega) \delta(\omega + \bar{\epsilon}_{\mathbf{k}'} - \bar{\epsilon}_{\mathbf{k}'+\mathbf{k}-\mathbf{p}}). \quad (\text{A3})$$

On the other hand, the unklapp scattering process occurs mainly at around EFS, i.e., $\mathbf{k}' \approx \mathbf{k}'_F$, therefore the momentum \mathbf{k}' in the effective spin propagator $P(\mathbf{k}, \mathbf{p} - \mathbf{k}, \mathbf{k}', \omega)$ can be approximately replaced by the

reduced effective spin propagator $\bar{P}(\mathbf{k}, \mathbf{p} - \mathbf{k}, \omega)$,

$$\bar{P}(\mathbf{k}, \mathbf{p} - \mathbf{k}, \omega) = \frac{1}{W_{\text{sp}}} P(\mathbf{k}, \mathbf{p} - \mathbf{k}, \mathbf{k}'_F, \omega), \quad (\text{A4})$$

where following the common practice, the scattering probability for two electrons has been normalized with the normalization factor $W_{\text{sp}}^2 = (1/N^2) \sum_{\mathbf{k}, \mathbf{p}} \int |\text{Im}\bar{P}(\mathbf{k}, \mathbf{p} - \mathbf{k}, \omega)|^2 d\omega$. Substituting above results in Eqs. (A3) and (A4) into Eq. (A1), the electron-electron collision in Eq. (A1) can be expressed explicitly as⁴¹,

$$\begin{aligned} I_{e-e} &= \frac{1}{N^2} \sum_{\mathbf{k}', \mathbf{p}} \frac{2}{T} |\bar{P}(\mathbf{k}, \mathbf{p} - \mathbf{k}, \bar{\epsilon}_{\mathbf{k}} - \bar{\epsilon}_{\mathbf{p}+\mathbf{G}})|^2 [\tilde{\Phi}(\mathbf{k}) - \tilde{\Phi}(\mathbf{p} + \mathbf{G})] n_F(\bar{\epsilon}_{\mathbf{k}}) n_F(\bar{\epsilon}_{\mathbf{k}'}) [1 - n_F(\bar{\epsilon}_{\mathbf{p}+\mathbf{G}})] [1 - n_F(\bar{\epsilon}_{\mathbf{k}'+\mathbf{k}-\mathbf{p}})] \\ &\times \int_{-\infty}^{\infty} d\omega \delta(\bar{\epsilon}_{\mathbf{k}} - \bar{\epsilon}_{\mathbf{p}+\mathbf{G}} - \omega) \delta(\omega + \bar{\epsilon}_{\mathbf{k}'} - \bar{\epsilon}_{\mathbf{k}'+\mathbf{k}-\mathbf{p}}) \\ &= \frac{1}{N^2} \sum_{\mathbf{k}', \mathbf{p}} \frac{2}{T} |\bar{P}(\mathbf{k}, \mathbf{p}, \bar{\epsilon}_{\mathbf{k}} - \bar{\epsilon}_{\mathbf{p}+\mathbf{k}+\mathbf{G}})|^2 [\tilde{\Phi}(\mathbf{k}) - \tilde{\Phi}(\mathbf{p} + \mathbf{k} + \mathbf{G})] n_F(\bar{\epsilon}_{\mathbf{k}}) n_F(\bar{\epsilon}_{\mathbf{k}'}) [1 - n_F(\bar{\epsilon}_{\mathbf{p}+\mathbf{k}+\mathbf{G}})] [1 - n_F(\bar{\epsilon}_{\mathbf{k}'-\mathbf{p}})] \\ &\times \int_{-\infty}^{\infty} d\omega \delta(\bar{\epsilon}_{\mathbf{k}} - \bar{\epsilon}_{\mathbf{p}+\mathbf{k}+\mathbf{G}} - \omega) \delta(\omega + \bar{\epsilon}_{\mathbf{k}'} - \bar{\epsilon}_{\mathbf{k}'-\mathbf{p}}). \end{aligned} \quad (\text{A5})$$

Now we replace the momentum \mathbf{k}' integration by an integration along EFS and one perpendicular to it, i.e., $(1/N) \sum_{\mathbf{k}'} = \int k' dk' d\theta_{k'} / (2\pi)^2$, where the $\theta_{k'}$ specifies a patch of EFS in the direction $\theta_{k'}$ as shown in Fig. 4,

and then the radial integration $\int dk'$ is replaced by an integral over $\int dk' = \int d\bar{\epsilon}_{\mathbf{k}'} / v_F$. In this case, the above electron-electron collision in Eq. (A5) can be simplified as,

$$\begin{aligned}
I_{e-e} &= \frac{1}{2\pi} \frac{2k_F}{Tv_F^2} \frac{1}{N} \sum_{\mathbf{p}} \frac{1}{|\mathbf{p}|} \int \frac{d\omega}{2\pi} |\bar{P}(\mathbf{k}, \mathbf{p}, \bar{\varepsilon}_{\mathbf{k}} - \bar{\varepsilon}_{\mathbf{p}+\mathbf{k}+\mathbf{G}})|^2 [\tilde{\Phi}(\mathbf{k}) - \tilde{\Phi}(\mathbf{p} + \mathbf{k} + \mathbf{G})] n_F(\bar{\varepsilon}_{\mathbf{k}}) [1 - n_F(\bar{\varepsilon}_{\mathbf{p}+\mathbf{k}+\mathbf{G}})] \\
&\times \omega [1 + n_B(\omega)] \delta(\bar{\varepsilon}_{\mathbf{k}} - \bar{\varepsilon}_{\mathbf{p}+\mathbf{k}+\mathbf{G}} - \omega).
\end{aligned} \tag{A6}$$

For the obtain of the above equation (A6), the following identity,

$$\int_{-\infty}^{+\infty} d\varepsilon n_F(\varepsilon - \omega) [1 - n_F(\varepsilon)] = \omega [1 + n_B(\omega)], \tag{A7}$$

has been used, where the appearance of the boson distribution function $n_B(\omega)$ in the right-hand side signals that we are describing a particle-hole effective spin excitation

which has the boson statistics⁴¹.

Now we turn to evaluate the momentum \mathbf{p} integration, which is quite similar to the evaluation of the momentum \mathbf{k}' integration in Eqs. (A5) and (A6). After a straightforward calculation for the momentum \mathbf{p} integration in Eq. (A6), the electron-electron collision term can be obtained explicitly as

$$I_{e-e} = \frac{1}{(2\pi)^2} \frac{2k_F^2}{Tv_F^3} \int \frac{d\theta'}{2\pi} \int \frac{d\omega}{2\pi} \frac{1}{p(\theta, \theta')} |\bar{P}[k(\theta), p(\theta, \theta'), \omega]|^2 [\Phi(\theta) - \Phi(\theta')] n_F(\bar{\varepsilon}_{k(\theta)}) [1 - n_F(\bar{\varepsilon}_{k(\theta)} - \omega)] \omega [1 + n_B(\omega)] \tag{A8}$$

where $\tilde{\Phi}(\mathbf{k})$ and $\tilde{\Phi}(\mathbf{p} + \mathbf{k} + \mathbf{G})$ in the right-hand of side have been replaced by $\Phi(\theta)$ and $\Phi(\theta')$, respectively, and at low-energy regime, the Boltzmann equation in Eq. (20) can be expressed as,

$$\begin{aligned}
e\mathbf{v}_F \cdot \mathbf{E} \frac{\partial n_F(\bar{\varepsilon}_{k(\theta)})}{\partial \bar{\varepsilon}_{k(\theta)}} &= \frac{1}{(2\pi)^2} \frac{2k_F^2}{Tv_F^3} \int \frac{d\theta'}{2\pi} \int \frac{d\omega}{2\pi} \frac{1}{p(\theta, \theta')} |\bar{P}[k(\theta), p(\theta, \theta'), \omega]|^2 [\Phi(\theta) - \Phi(\theta')] \\
&\times n_F(\bar{\varepsilon}_{k(\theta)}) [1 - n_F(\bar{\varepsilon}_{k(\theta)} - \omega)] \omega [1 + n_B(\omega)].
\end{aligned} \tag{A9}$$

Integrating both the left-hand and right-hand sides over the energy $\bar{\varepsilon}_{k(\theta)}$, the Boltzmann equation in Eq. (A9) can be obtained explicitly as,

$$\begin{aligned}
e\mathbf{v}_F \cdot \mathbf{E} &= -\frac{1}{(2\pi)^2} \frac{2k_F^2}{Tv_F^3} \int \frac{d\theta'}{2\pi} \int \frac{d\omega}{2\pi} \frac{1}{p(\theta, \theta')} |\bar{P}[k(\theta), p(\theta, \theta'), \omega]|^2 [\Phi(\theta) - \Phi(\theta')] \omega^2 n_B(\omega) [1 + n_B(\omega)] \\
&= -2 \int \frac{d\theta'}{2\pi} \zeta(\theta') F(\theta, \theta') [\Phi(\theta) - \Phi(\theta')],
\end{aligned} \tag{A10}$$

which is the same as quoted in Eq. (23) of the main text.

Appendix B: Derivation of function $I_{jj'}(\theta, \theta', \mathbf{q}, \mathbf{q}')$

In this Appendix, we sketch the derivation of the function $I_{jj'}(\theta, \theta', \mathbf{q}, \mathbf{q}')$ in Eq. (36) of the main text. For a convenience in the following discussions, we define the functions: $C = C_j(\theta, \theta', \mathbf{q})$, $C' = C_{j'}(\theta, \theta', \mathbf{q}')$, and $I(C, C') = I_{jj'}(\theta, \theta', \mathbf{q}, \mathbf{q}')$. In this case, the function $I_{jj'}(\theta, \theta', \mathbf{q}, \mathbf{q}')$ in Eq. (36) of the main text can be rewritten

in the complex-plane as,

$$I_z(C, C') = \int \frac{dz}{i2\pi} \frac{e^z}{(e^z - 1)^2} \frac{z^2}{[z^2 - C^2][z^2 - C'^2]}, \tag{B1}$$

with the closed integration path in the upper complex-plane, and then this integration along the real axis can be obtained as,

$$\begin{aligned}
I(C, C') &= P \int_{-\infty}^{\infty} \frac{dx}{i2\pi} \frac{e^x}{(e^x - 1)^2} \frac{x^2}{[x^2 - C^2][x^2 - C'^2]} = \text{res}[z = i\omega_n = i2\pi n (n \in N^+)] \\
&+ \frac{1}{2} \sum_{z_0} \lim_{z \rightarrow z_0} (z - z_0) \frac{e^z}{(e^z - 1)^2} \frac{z^2}{[z^2 - C^2][z^2 - C'^2]},
\end{aligned} \tag{B2}$$

where $z_0 = i\omega_n$, $z_0 = \pm C$, and $z_0 = \pm C'$ are the poles. With the help of the above results in Eq. (B2), the function $I(C, C')$ in Eq. (36) can be expressed in terms of the residues of the corresponding poles as,

$$\begin{aligned} I(C, C') &= P \int_{-\infty}^{\infty} \frac{dx}{i2\pi} \frac{e^x}{(e^x - 1)^2} \frac{x^2}{[x^2 - C^2][x^2 - C'^2]} = -2 \sum_{n>0} \frac{i\omega_n [i\omega_n^4 - C^2 C'^2]}{[i\omega_n^2 - C^2]^2 [i\omega_n^2 - C'^2]^2} \\ &= - \sum_n \frac{i|\omega_n| [i\omega_n^4 - C^2 C'^2]}{[i\omega_n^2 - C^2]^2 [i\omega_n^2 - C'^2]^2}. \end{aligned} \quad (\text{B3})$$

For obtaining the above result in Eq. (B3), the following identities,

$$\lim_{z \rightarrow 0} z \frac{e^z}{(e^z - 1)^2} \frac{z^2}{[z^2 - C^2][z^2 - C'^2]} = 0, \quad (\text{B4a})$$

$$\lim_{z \rightarrow \pm C} (z - \pm C) \frac{e^z}{(e^z - 1)^2} \frac{z^2}{[z^2 - C^2][z^2 - C'^2]} = \pm \frac{1}{2} \frac{e^C}{[e^C - 1]^2} \frac{C}{C^2 - C'^2}, \quad (\text{B4b})$$

$$\lim_{z \rightarrow \pm C'} (z - \pm C') \frac{e^z}{(e^z - 1)^2} \frac{z^2}{[z^2 - C^2][z^2 - C'^2]} = \pm \frac{1}{2} \frac{e^{C'}}{[e^{C'} - 1]^2} \frac{C'}{C'^2 - C^2}, \quad (\text{B4c})$$

$$\text{res}[z = i\omega_n = i2\pi n (n \in N^+)] = -2 \frac{i\omega_n [i\omega_n^4 - C^2 C'^2]}{[i\omega_n^2 - C^2]^2 [i\omega_n^2 - C'^2]^2}, \quad (\text{B4d})$$

have been used. We now introduce the following integration,

$$\bar{I}_z(C, C') = \int \frac{dz}{i2\pi} \frac{|z|[z^4 - C^2 C'^2]}{[z^2 - C^2]^2 [z^2 - C'^2]^2} n_B(z), \quad (\text{B5})$$

with the integration path along the closed path at infinity in the complex-plane, which can be derived directly as,

$$\bar{I}_z(C, C') = \sum_n \frac{|\omega_n| [i\omega_n^4 - C^2 C'^2]}{[i\omega_n^2 - C^2]^2 [i\omega_n^2 - C'^2]^2} + \sum_{z_0} \lim_{z \rightarrow z_0} \frac{d}{dz} (z - z_0)^2 \frac{|z|[z^4 - C^2 C'^2]}{[z^2 - C^2]^2 [z^2 - C'^2]^2} n_B(z) = 0, \quad (\text{B6})$$

where the poles are located at $z_0 = \pm C$ and $z_0 = \pm C'$, while the derivative in the above equation (B6) can be calculated straightforwardly as,

$$\begin{aligned} \frac{d}{dz} (z - z_0)^2 \frac{|z|[z^4 - C^2 C'^2]}{[z^2 - C^2]^2 [z^2 - C'^2]^2} n_B(z) \Big|_{z \rightarrow z_0} &= \frac{d}{dz} \frac{|z|[z^4 - C^2 C'^2]}{[z + z_0]^2 [z^2 - z_0'^2]^2} n_B(z) \Big|_{z \rightarrow z_0} \\ &= \frac{z_0^2 (z_0^2 - z_0'^2)^2 [|z_0|' (z_0^4 - C^2 C'^2) + 4|z_0| z_0^3] - |z_0| z_0 (z_0^2 - z_0'^2) (z_0^4 - C^2 C'^2) (5z_0^2 - z_0'^2)}{4z_0^4 (z_0^2 - z_0'^2)^4} \frac{1}{e^{z_0} - 1} \\ &\quad - \frac{|z_0| (z_0^4 - C^2 C'^2)}{4z_0^2 (z_0^2 - z_0'^2)^2} \frac{e^{z_0}}{(e^{z_0} - 1)^2}, \end{aligned} \quad (\text{B7})$$

and then the residues in Eq. (B6) corresponding to the poles at $z_0 = \pm C$ and $z_0 = \pm C'$ are derived explicitly as,

$$\text{res}(z_0 = C) = \text{res}(z_0 = -C) = \frac{C}{4(C^2 - C'^2)} \frac{e^C}{(e^C - 1)^2}, \quad (\text{B8a})$$

$$\text{res}(z_0 = C') = \text{res}(z_0 = -C') = \frac{C'}{4(C'^2 - C^2)} \frac{e^{C'}}{(e^{C'} - 1)^2}, \quad (\text{B8b})$$

respectively. With the help of the above results of the residues, the following identity is obtained explicitly,

$$- \sum_n \frac{|\omega_n| (i\omega_n^4 - C^2 C'^2)}{(i\omega_n^2 - C^2)^2 (i\omega_n^2 - C'^2)^2} = \frac{1}{2(C^2 - C'^2)} \left[\frac{C e^C}{(e^C - 1)^2} - \frac{C' e^{C'}}{(e^{C'} - 1)^2} \right]. \quad (\text{B9})$$

Substituting the above result in Eq. (B9) into Eq. (B2), the function $I(C, C')$ can be obtained explicitly as,

$$I(C, C') = \frac{i}{2[C^2 - C'^2]} \left(\frac{C e^C}{[e^C - 1]^2} - \frac{C' e^{C'}}{[e^{C'} - 1]^2} \right), \quad (\text{B10})$$

which is the same as quoted in Eq. (39) of the main text.

-
- * These authors contributed equally to this work
† Corresponding author. E-mail: spfeng@bnu.edu.cn
- ¹ See, e.g., the review, M. Fujita, H. Hiraka, M. Matsuda, M. Matsuura, J. M. Tranquada, S. Wakimoto, G. Xu, and K. Yamada, Progress in neutron scattering studies of spin excitations in high- T_c cuprates, *J. Phys. Soc. Jpn.* **81**, 011007 (2012).
 - ² J. G. Bednorz and K. A. Müller, Possible high T_c superconductivity in the Ba-La-Cu-O system, *Z. Phys. B* **64**, 189 (1986).
 - ³ See, e.g., the review, I. M. Vishik, Photoemission perspective on pseudogap, superconducting fluctuations, and charge order in cuprates: a review of recent progress, *Rep. Prog. Phys.* **81**, 062501 (2018).
 - ⁴ See, e.g., the review, J. C. Campuzano, M. R. Norman, M. Randeria, Photoemission in the high- T_c superconductors, in *Physics of Superconductors*, vol. II, edited by K. H. Bennemann and J. B. Ketterson (Springer, Berlin Heidelberg New York, 2004), p. 167.
 - ⁵ See, e.g., the review, A. Damascelli, Z. Hussain, and Z.-X. Shen, Angle-resolved photoemission studies of the cuprate superconductors, *Rev. Mod. Phys.* **75**, 473 (2003).
 - ⁶ See, e.g., the review, J. Fink, S. Borisenko, A. Kordyuk, A. Koitzsch, J. Geck, V. Zabalotnyy, M. Knupfer, B. Büchner, and H. Berger, Dressing of the charge carriers in high- T_c superconductors, in *Lecture Notes in Physics*, vol. 715, edited by S. Hüfner (Springer-Verlag Berlin Heidelberg, 2007), p. 295.
 - ⁷ See, e.g., the review, B. Keimer, S. A. Kivelson, M. R. Norman, S. Uchida, and J. Zaanen, From quantum matter to high-temperature superconductivity in copper oxides, *Nature* **518**, 179 (2015).
 - ⁸ See, e.g., the review, N. E. Hussey, Phenomenology of the normal state in-plane transport properties of high- T_c cuprates, *J. Phys.: Condens. Matter* **20**, 123201 (2008).
 - ⁹ See, e.g., the review, T. Timusk and B. Statt, The pseudogap in high-temperature superconductors: an experimental survey, *Rep. Prog. Phys.* **62**, 61 (1999).
 - ¹⁰ See, e.g., the review, M. A. Kastner, R. J. Birgeneau, G. Shirane, and Y. Endoh, Magnetic, transport, and optical properties of monolayer copper oxides, *Rev. Mod. Phys.* **70**, 897 (1998).
 - ¹¹ Y. Ando, S. Komiya, K. Segawa, S. Ono, and Y. Kurita, Electronic phase diagram of high- T_c cuprate superconductors from a mapping of the in-plane resistivity curvature, *Phys. Rev. Lett.* **93**, 267001 (2004).
 - ¹² N. Barišić, M. K. Chan, Y. Li, G. Yu, X. Zhao, M. Dressel, A. Smontara, and M. Greven, Universal sheet resistance and revised phase diagram of the cuprate high-temperature superconductors, *Proc. Natl. Acad. Sci. USA* **110**, 12235 (2013).
 - ¹³ D. Pelc, M. J. Veit, C. J. Dorow, Y. Ge, N. Barišić, and M. Greven, Resistivity phase diagram of cuprates revisited, *Phys. Rev. B* **102**, 075114 (2020).
 - ¹⁴ See, e.g., J. R. Schrieffer, *Theory of Superconductivity*, Benjamin, New York, 1964.
 - ¹⁵ See, e.g., A. A. Abrikosov, *Fundamentals of the Theory of Metals*, Elsevier Science Publishers B. V., 1988.
 - ¹⁶ See, e.g., G. D. Mahan, *Many-Particle Physics*, (Plenum Press, New York, 1981).
 - ¹⁷ See, e.g., the review, P. B. Allen, Z. Fisk, and A. Migliori, Normal state transport and elastic properties of high T_c materials and related compounds, in *Physical Properties of High Temperature Superconductors I*, edited by D. M. Ginsberg (World Scientific, Singapore, 1989), p. 213.
 - ¹⁸ M. Gurvitch and A. T. Fiory, Resistivity of $\text{La}_{1.825}\text{Sr}_{0.175}\text{CuO}_4$ and $\text{YBa}_2\text{Cu}_3\text{O}_7$ to 1100 K: absence of saturation and its implications, *Phys. Rev. Lett.* **59**, 1337 (1987).
 - ¹⁹ H. Takagi, B. Batlogg, H. L. Kao, J. Kwo, R. J. Cava, J. J. Krajewski, and W. F. Peck, Jr., Systematic evolution of temperature-dependent resistivity in $\text{La}_{2-x}\text{Sr}_x\text{CuO}_4$, *Phys. Rev. Lett.* **69**, 2975 (1992).
 - ²⁰ S. Martin, A. T. Fiory, R. M. Fleming, L. F. Schneemeyer, and J. V. Waszczak, Normal-state transport properties of $\text{Bi}_{2+x}\text{Sr}_{2-y}\text{Cu}_{6\pm\delta}$ crystals, *Phys. Rev. B* **41**, 846 (1990).
 - ²¹ D. Mandrus, L. Forro, C. Kendziora, and L. Mihaly, Resistivity study of $\text{Bi}_2\text{Sr}_2\text{Ca}_{1-x}\text{Y}_x\text{Cu}_2\text{O}_8$ single crystals, *Phys. Rev. B* **45**, 12640 (1992).
 - ²² Y. Ando, A. N. Lavrov, S. Komiya, K. Segawa, and X. F. Sun, Mobility of the doped holes and the antiferromagnetic correlations in underdoped high- T_c cuprates, *Phys. Rev. Lett.* **87**, 017001 (2001).
 - ²³ R. Daou, N. Doiron-Leyraud, D. LeBoeuf, S. Y. Li, F. Laliberté, O. Cyr-Choinière, Y. J. Jo, L. Balicas, J.-Q. Yan, J.-S. Zhou, J. B. Goodenough, and L. Taillefer, Linear temperature dependence of resistivity and change in the Fermi surface at the pseudogap critical point of a high- T_c superconductor, *Nat. Phys.* **5**, 31 (2009).
 - ²⁴ R. A. Cooper, Y. Wang, B. Vignolle, O. J. Lipscombe, S. M. Hayden, Y. Tanabe, T. Adachi, Y. Koike, M. Nohara, H. Takagi, C. Proust, N. E. Hussey, Anomalous criticality in the electrical resistivity of $\text{La}_{2-x}\text{Sr}_x\text{CuO}_4$, *Science* **323**, 603 (2009).
 - ²⁵ A. Legros, S. Benhabib, W. Tabis, F. Laliberté, M. Dion, M. Lizaire, B. Vignolle, D. Vignolles, H. Raffy, Z. Z. Li, P. Auban-Senzier, N. Doiron-Leyraud, P. Fournier, D. Colson, L. Taillefer, and C. Proust, Universal T -linear resistivity and Planckian dissipation in overdoped cuprates, *Nat. Phys.* **15**, 142 (2019).
 - ²⁶ J. Yuan, Q. Chen, K. Jiang, Z. Feng, Z. Lin, H. Yu, G. He, J. Zhang, X. Jiang, X. Zhang, Y. Shi, Y. Zhang, M. Qin, Z. Cheng, N. Tamura, Y.-F. Yang, T. Xiang, J. Hu, I. Takeuchi, K. Jin, and Z. Zhao, Scaling of the strange-metal scattering in unconventional superconductors, *Nature* **602**, 431 (2022).
 - ²⁷ J. Ayres, M. Berben, M. Čulo, Y.-T. Hsu, E. van Heumen, Y. Huang, J. Zaanen, T. Kondo, T. Takeuchi, J. R. Cooper, C. Putzke, S. Friedemann, A. Carrington, and N. E. Hussey, Incoherent transport across the strange-metal regime of overdoped cuprates, *Nature* **595**, 661 (2021).

- ²⁸ G. Grissonnanche, Y. Fang, A. Legros, S. Verret, F. Laliberté, C. Collignon, J. Zhou, D. Graf, P. A. Goddard, L. Taillefer, and B. J. Ramshaw, Linear-in temperature resistivity from an isotropic Planckian scattering rate, *Nature* **595**, 667 (2021).
- ²⁹ C. M. Varma, P. B. Littlewood, S. Schmitt-Rink, E. Abrahams, and A. E. Ruckenstein, Phenomenology of the normal state of Cu-O high-temperature superconductors, *Phys. Rev. Lett.* **63**, 1996 (1989).
- ³⁰ See, e.g., the review, C. M. Varma, Quantum-critical fluctuations in 2D metals: strange metals and superconductivity in antiferromagnets and in cuprates, *Rep. Prog. Phys.* **79** 082501 (2016)
- ³¹ See, e.g., the review, C. M. Varma, Colloquium: Linear in temperature resistivity and associated mysteries including high temperature superconductivity, *Rev. Mod. Phys.* **92**, 031001 (2020).
- ³² K. Damle and S. Sachdev, Nonzero-temperature transport near quantum critical points, *Phys. Rev. B* **56**, 8714 (1997).
- ³³ S. Sachdev, *Quantum Phase Transitions*, (Cambridge University Press, 1999).
- ³⁴ J. Zaanen, Why the temperature is high, *Nature* **430**, 512 (2004).
- ³⁵ L. Dell’Anna and W. Metzner, Electrical resistivity near Pomeranchuk instability in two dimensions, *Phys. Rev. Lett.* **98**, 136402 (2007).
- ³⁶ F. D. M. Haldane, Fermi-surface geometry and “Planckian dissipation”, arXiv:1811.12120.
- ³⁷ See, e.g., the review, J. Zaanen, Planckian dissipation, minimal viscosity and the transport in cuprate strange metals, *SciPost Phys.* **6**, 061 (2019).
- ³⁸ See, e.g., the review, S. A. Hartnoll and A. P. Mackenzie, Colloquium: Planckian dissipation in metals, *Rev. Mod. Phys.* **94**, 041002 (2022).
- ³⁹ N. E. Hussey, The normal state scattering rate in high- T_c cuprates, *Eur. Phys. J. B* **31**, 495 (2003).
- ⁴⁰ T. M. Rice, N. J. Robinson, and A. M. Tsvelik, Umklapp scattering as the origin of T -linear resistivity in the normal state of high- T_c cuprate superconductors, *Phys. Rev. B* **96**, 220502(R) (2017).
- ⁴¹ P. A. Lee, Low-temperature T -linear resistivity due to umklapp scattering from a critical mode, *Phys. Rev. B* **104**, 035140 (2021).
- ⁴² C. Honerkamp, M. Salmhofer, N. Furukawa, and T. M. Rice, Breakdown of the Landau-Fermi liquid in two dimensions due to umklapp scattering, *Phys. Rev. B* **63**, 035109 (2001).
- ⁴³ S. A. Hartnoll and D. M. Hofman, Locally critical resistivities from umklapp scattering, *Phys. Rev. Lett.* **108**, 241601 (2012).
- ⁴⁴ W. Tabiś, P. Popčević, B. Klebel-Knobloch, I. Bialo, C. M. N. Kumar, B. Vignolle, M. Greven, N. Barišić, Arc-to-pocket transition and quantitative understanding of transport properties in cuprate superconductors, arXiv:2106.07457.
- ⁴⁵ Y. Liu, Y. Lan, and S. Feng, Peak structure in the self-energy of cuprate superconductors, *Phys. Rev. B* **103**, 024525 (2021); S. Tan, Y. Liu, Y. Mou, and S. Feng, Anisotropic dressing of electrons in electron-doped cuprate superconductors, *Phys. Rev. B* **103**, 014503 (2021).
- ⁴⁶ Z. Cao, X. Ma, Y. Liu, H. Guo, and S. Feng, Characteristic energy of the nematic-order state and its connection to enhancement of superconductivity in cuprate superconductors, *Phys. Rev. B* **104**, 224503 (2021); Z. Cao, Y. Liu, H. Guo, and S. Feng, Enhancement of superconductivity by electronic nematicity in cuprate superconductors, *Phil. Mag.* **102**, 918 (2022).
- ⁴⁷ M. Zeng, X. Li, Y. Wang, and S. Feng, Influence of impurities on the electronic structure in cuprate superconductors, *Phys. Rev. B* **106**, 054512 (2022).
- ⁴⁸ S. Feng, D. Gao, and H. Zhao, Charge order driven by Fermi-arc instability and its connection with pseudogap in cuprate superconductors, *Phil. Mag.* **96**, 1245 (2016); H. Zhao, D. Gao, and S. Feng, Pseudogap-generated a coexistence of Fermi arcs and Fermi pockets in cuprate superconductors, *Physica C* **534**, 1 (2017); X. Ma, Z. Cao, and S. Feng, unpublished.
- ⁴⁹ P. W. Anderson, The resonating valence bond state in La_2CuO_4 and superconductivity, *Science* **235**, 1196 (1987).
- ⁵⁰ See, e.g., the review, L. Yu, Many-body problems in high temperature superconductors, in *Recent Progress in Many-Body Theories*, edited by T. L. Ainsworth, C. E. Campbell, B. E. Clements, and E. Krotschek (Plenum, New York, 1992), Vol. **3**, p. 157.
- ⁵¹ See, e.g., the review, P. A. Lee, N. Nagaosa, and X.-G. Wen, Doping a Mott insulator: Physics of high-temperature superconductivity, *Rev. Mod. Phys.* **78**, 17 (2006).
- ⁵² See, e.g., the review, B. Edegger, V. N. Muthukumar, and C. Gros, Gutzwiller–RVB theory of high-temperature superconductivity: Results from renormalized mean-field theory and variational Monte Carlo calculations, *Adv. Phys.* **56**, 927 (2007).
- ⁵³ J. Spalek, M. Fidrysiak, M. Zegrodnik, and A. Biborski, Superconductivity in high- T_c and related strongly correlated systems from variational perspective: Beyond mean field theory, *Phys. Rep.* **959**, 1 (2022).
- ⁵⁴ L. Zhang, J. K. Jain, and V. J. Emery, Importance of the local constraint in slave-boson theories, *Phys. Rev. B* **47**, 3368 (1993).
- ⁵⁵ S. Feng, J. Qin, and T. Ma, A gauge invariant dressed holon and spinon description of the normal state of underdoped cuprates, *J. Phys.: Condens. Matter* **16**, 343 (2004); S. Feng, Z. B. Su, and L. Yu, Fermion-spin transformation to implement the charge-spin separation, *Phys. Rev. B* **49**, 2368 (1994).
- ⁵⁶ See, e.g., the review, S. Feng, Y. Lan, H. Zhao, L. Kuang, L. Qin, and X. Ma, Kinetic-energy-driven superconductivity in cuprate superconductors, *Int. J. Mod. Phys. B* **29**, 1530009 (2015).
- ⁵⁷ S. Feng, Kinetic energy driven superconductivity in doped cuprates, *Phys. Rev. B* **68**, 184501 (2003); S. Feng, T. Ma, and H. Guo, Magnetic nature of superconductivity in doped cuprates, *Physica C* **436**, 14 (2006).
- ⁵⁸ S. Feng, H. Zhao, and Z. Huang, Two gaps with one energy scale in cuprate superconductors, *Phys. Rev. B* **85**, 054509 (2012); *Phys. Rev. B* **85**, 099902(E) (2012).
- ⁵⁹ S. Feng, L. Kuang, and H. Zhao, Electronic structure of cuprate superconductors in a full charge-spin recombination scheme, *Physica C* **517**, 5 (2015).
- ⁶⁰ D. J. Scalapino, E. Loh, Jr., and J. E. Hirsch, d -wave pairing near a spin-density-wave instability, *Phys. Rev. B* **34**, 8190 (1986).
- ⁶¹ K. Miyake, S. Schmitt-Rink, and C. M. Varma, Spin-fluctuation-mediated even-parity pairing in heavy-fermion

- superconductors, *Phys. Rev. B* **34**, 6554 (1986).
- ⁶² P. Monthoux, A. V. Balatsky, and D. Pines, Toward a theory of high-temperature superconductivity in the antiferromagnetically correlated cuprate oxides, *Phys. Rev. Lett.* **67**, 3448 (1991); P. Monthoux and D. Pines, $\text{YBa}_2\text{Cu}_3\text{O}_7$: A nearly antiferromagnetic Fermi liquid, *Phys. Rev. B* **47**, 6069 (1993).
- ⁶³ P. Monthoux, D. Pines, and G. G. Lonzarich, Superconductivity without phonons, *Nature* **450**, 1177 (2007).
- ⁶⁴ G. M. Eliashberg, Interactions between electrons and lattice vibrations in a superconductor, *Sov. Phys. JETP* **11**, 696 (1960).
- ⁶⁵ J. Brinckmann and P. A. Lee, Renormalized mean-field theory of neutron scattering in cuprate superconductors, *Phys. Rev. B* **65**, 014502 (2001).
- ⁶⁶ F. Restrepo, J. Zhao, J. C. Campuzano, and U. Chatterjee, Temperature and carrier concentration dependence of Fermi arcs in moderately underdoped $\text{Bi}_2\text{Sr}_2\text{CaCu}_2\text{O}_{8+\delta}$ cuprate high-temperature superconductors: A joint density of states perspective, *Phys. Rev. B* **107**, 174519 (2023).
- ⁶⁷ M. R. Norman, H. Ding, M. Randeria, J. C. Campuzano, T. Yokoya, T. Takeuchi, T. Takahashi, T. Mochiku, K. Kadowaki, P. Guptasarma, and D. G. Hinks, Destruction of the Fermi surface in underdoped high- T_c superconductors, *Nature* **392**, 157 (1998).
- ⁶⁸ M. Shi, J. Chang, S. Pailh es, M. R. Norman, J. C. Campuzano, M. M ansson, T. Claesson, O. Tjernberg, A. Bendounan, L. Patthey, N. Momono, M. Oda, M. Ido, C. Mudry, and J. Mesot, Coherent d -wave superconducting gap in underdoped $\text{La}_{2-x}\text{Sr}_x\text{CuO}_4$ by angle-resolved photoemission spectroscopy, *Phys. Rev. Lett.* **101**, 047002 (2008).
- ⁶⁹ Y. Sassa, M. Radovi c, M. M ansson, E. Razzoli, X. Y. Cui, S. Pailh es, S. Guerrero, M. Shi, P. R. Willmott, F. Miletto Granozio, J. Mesot, M. R. Norman, and L. Patthey, Ortho-II band folding in $\text{YBa}_2\text{Cu}_3\text{O}_{7-\delta}$ films revealed by angle-resolved photoemission, *Phys. Rev. B* **83**, 140511(R) (2011).
- ⁷⁰ J. Q. Meng, M. Brunner, K.-H. Kim, H.-G. Lee, S.-I. Lee, J. S. Wen, Z. J. Xu, G. D. Gu, and G.-H. Gweon, Momentum-space electronic structures and charge orders of the high-temperature superconductors $\text{Ca}_{2-x}\text{Na}_x\text{CuO}_2\text{Cl}_2$ and $\text{Bi}_2\text{Sr}_2\text{CaCu}_2\text{O}_{8+\delta}$, *Phys. Rev. B* **84**, 060513 (R) (2011).
- ⁷¹ M. Horio, T. Adachi, Y. Mori, A. Takahashi, T. Yoshida, H. Suzuki, L. C. C. Ambolode II, K. Okazaki, K. Ono, H. Kumigashira, H. Anzai, M. Arita, H. Namatame, M. Taniguchi, D. Ootsuki, K. Sawada, M. Takahashi, T. Mizokawa, Y. Koike, and A. Fujimori, Suppression of the antiferromagnetic pseudogap in the electron-doped high-temperature superconductor by protect annealing, *Nat. Commun.* **7**, 10567 (2016).
- ⁷² B. Loret, Y. Gallais, M. Cazayous, R. D. Zhong, J. Schneeloch, G. D. Gu, A. Fedorov, T. K. Kim, S. V. Borisenko, and A. Sacuto, Raman and ARPES combined study on the connection between the existence of the pseudogap and the topology of the Fermi surface in $\text{Bi}_2\text{Sr}_2\text{CaCu}_2\text{O}_{8+\delta}$, *Phys. Rev. B* **97**, 174521 (2018).
- ⁷³ S. D. Chen, M. Hashimoto, Y. He, D. Song, K. J. Xu, J. F. He, T. P. Devereaux, H. Eisaki, D. H. Lu, J. Zaanen, and Z. -X. Shen, Incoherent strange metal sharply bounded by a critical doping in $\text{Bi}2212$, *Science* **366**, 1099 (2019).
- ⁷⁴ B. Loret, S. Sakai, S. Benhabib, Y. Gallais, M. Cazayous, M. A. Measson, R. D. Zhong, J. Schneeloch, G. D. Gu, A. Forget, D. Colson, I. Paul, M. Civelli, and A. Sacuto, Vertical temperature boundary of the pseudogap under the superconducting dome in the phase diagram of $\text{Bi}_2\text{Sr}_2\text{CaCu}_2\text{O}_{8+\delta}$, *Phys. Rev. B* **96**, 094525 (2017).
- ⁷⁵ A. Kaminski, T. Kondo, T. Takeuchi, and G. Gu, Pairing, pseudogap and Fermi arcs in cuprates, *Phil. Mag.* **95**, 453 (2015).
- ⁷⁶ R. Comin, A. Frano, M. M. Yee, Y. Yoshida, H. Eisaki, E. Schierle, E. Weschke, R. Sutarto, F. He, A. Soumyanarayanan, Yang He, M. L. Tacon, I. S. Elfimov, Jennifer E. Hoffman, G. A. Sawatzky, B. Keimer, and A. Damascelli, Charge order driven by Fermi-arc instability in $\text{Bi}_2\text{Sr}_{2-x}\text{La}_x\text{CuO}_{6+\delta}$, *Science* **343**, 390 (2014).
- ⁷⁷ K. Fujita, C. K. Kim, I. Lee, J. Lee, M. H. Hamidian, I. A. Fermo, S. Mukhopadhyay, H. Eisaki, S. Uchida, M. J. Lawler, E.-A. Kim, and J. C. Davis, Simultaneous transitions in cuprate momentum-space topology and electronic symmetry breaking, *Science* **344**, 612 (2014).
- ⁷⁸ See, e.g., the review, S. H ufner, M. A. Hossain, A. Damascelli, and G. A. Sawatzky, Two gaps make a high-temperature superconductor?, *Rep. Prog. Phys.* **71**, 062501 (2008), and references therein.
- ⁷⁹ Y. He, Y. Yin, M. Zech, A. Soumyanarayanan, M. M. Yee, T. Williams, M. C. Boyer, K. Chatterjee, W. D. Wise, I. Zeljkovic, T. Kondo, T. Takeuchi, H. Ikuta, P. Mistark, R. S. Markiewicz, A. Bansil, S. Sachdev, E. W. Hudson, and J. E. Hoffman, Fermi surface and pseudogap evolution in a cuprate superconductor, *Science* **344**, 608 (2014).
- ⁸⁰ U. Chatterjee, M. Shi, A. Kaminski, A. Kanigel, H. M. Fretwell, K. Terashima, T. Takahashi, S. Rosenkranz, Z. Z. Li, H. Raffy, A. Santander-Syro, K. Kadowaki, M. R. Norman, M. Randeria, and J. C. Campuzano, Nondispersive Fermi arcs and the absence of charge ordering in the pseudogap phase of $\text{Bi}_2\text{Sr}_2\text{CaCu}_2\text{O}_{8+\delta}$, *Phys. Rev. Lett.* **96**, 107006 (2006).
- ⁸¹ See, e.g., the review, Riccardo Comin and Andrea Damascelli, Resonant X-ray scattering studies of charge order in cuprates, *Annu. Rev. Condens. Matter Phys.* **7**, 369 (2016).
- ⁸² See, e.g., the review, J.-X. Yin, S. H. Pan, M. Z. Hasan, Probing topological quantum matter with scanning tunnelling microscopy, *Nat. Rev. Phys.* **3**, 249 (2021).
- ⁸³ S. H. Pan, J. P.  Neal, R. L. Badzey, C. Chamon, H. Ding, J. R. Engelbrecht, Z. Wang, H. Eisaki, S. Uchida, A. K. Gupta, K.-W. Ng, E. W. Hudson, K. M. Lang, and J. C. Davis, Microscopic electronic inhomogeneity in the high- T_c superconductor $\text{Bi}_2\text{Sr}_2\text{CaCu}_2\text{O}_{8+x}$, *Nature* **413**, 282 (2001).
- ⁸⁴ S. Mukhopadhyay, R. Sharma, C. K. Kim, S. D. Edkins, M. H. Hamidian, H. Eisaki, S. Uchida, E.-A. Kim, M. J. Lawler, A. P. Mackenzie, J. C. S. Davis, and K. Fujita, Evidence for a vestigial nematic state in the cuprate pseudogap phase, *Proc. Natl. Acad. Sci.* **116**, 13249 (2019).
- ⁸⁵ D. S. Dessau, B. O. Wells, Z.-X. Shen, W. E. Spicer, A. J. Arko, R. S. List, D. B. Mitzi, and A. Kapitulnik, Anomalous spectral weight transfer at the superconducting transition of $\text{Bi}_2\text{Sr}_2\text{CaCu}_2\text{O}_{8+\delta}$, *Phys. Rev. Lett.* **66**, 2160 (1991).
- ⁸⁶ M. R. Norman, H. Ding, J. C. Campuzano, T. Takeuchi, M. Randeria, T. Yokoya, T. Takahashi, T. Mochiku, and K. Kadowaki, Unusual dispersion and line shape of the su-

- perconducting state spectra of $\text{Bi}_2\text{Sr}_2\text{CaCu}_2\text{O}_{8+\delta}$, Phys. Rev. Lett. **79**, 3506 (1997).
- ⁸⁷ J. C. Campuzano, H. Ding, M. R. Norman, H. M. Fretwell, M. Randeria, A. Kaminski, J. Mesot, T. Takeuchi, T. Sato, T. Yokoya, T. Takahashi, T. Mochiku, K. Kadowaki, P. Guptasarma, D. G. Hinks, Z. Konstantinovic, Z. Z. Li, and H. Raffy, Electronic spectra and their relation to the (π, π) collective mode in high- T_c superconductors, Phys. Rev. Lett. **83**, 3709 (1999).
- ⁸⁸ J. Wei, Y. Zhang, H. W. Ou, B. P. Xie, D. W. Shen, J. F. Zhao, L. X. Yang, M. Arita, K. Shimada, H. Namatame, M. Taniguchi, Y. Yoshida, H. Eisaki, and D. L. Feng, Superconducting coherence peak in the electronic excitations of a single-layer $\text{Bi}_2\text{Sr}_{1.6}\text{La}_{0.4}\text{CuO}_{6+\delta}$ cuprate superconductor, Phys. Rev. Lett. **101**, 097005 (2008).
- ⁸⁹ Daixiang Mou, Adam Kaminski, and Genda Gu, Direct observation of self-energy signatures of the resonant collective mode in $\text{Bi}_2\text{Sr}_2\text{CaCu}_2\text{O}_{8+\delta}$, Phys. Rev. B **95**, 174501 (2017).
- ⁹⁰ A. Kaminski, M. Randeria, J. C. Campuzano, M. R. Norman, H. Fretwell, J. Mesot, T. Sato, T. Takahashi, and K. Kadowaki, Renormalization of spectral line shape and dispersion below T_c in $\text{Bi}_2\text{Sr}_2\text{CaCu}_2\text{O}_{8+\delta}$, Phys. Rev. Lett. **86**, 1070 (2001).
- ⁹¹ X. J. Zhou, T. Yoshida, A. Lanzara, P. V. Bogdanov, S. A. Kellar, K. M. Shen, W. L. Yang, F. Ronning, T. Sasagawa, T. Kakeshita, T. Noda, H. Eisaki, S. Uchida, C. T. Lin, F. Zhou, J. W. Xiong, W. X. Ti, Z. X. Zhao, A. Fujimori, Z. Hussain, and Z.-X. Shen, Universal nodal Fermi velocity, Nature **423**, 398 (2003).
- ⁹² H. Anzai, A. Ino, T. Kamo, T. Fujita, M. Arita, H. Namatame, M. Taniguchi, A. Fujimori, Z.-X. Shen, M. Ishikado, and S. Uchida, Energy-dependent enhancement of the electron-coupling spectrum of the underdoped $\text{Bi}_2\text{Sr}_2\text{CaCu}_2\text{O}_{8+\delta}$ superconductor, Phys. Rev. Lett. **105**, 227002 (2010).
- ⁹³ J. He, W. Zhang, J. M. Bok, D. Mou, L. Zhao, Y. Peng, S. He, G. Liu, X. Dong, J. Zhang, J. S. Wen, Z. J. Xu, G. D. Gu, X. Wang, Q. Peng, Z. Wang, S. Zhang, F. Yang, C. Chen, Z. Xu, H.-Y. Choi, C. M. Varma, and X. J. Zhou, Coexistence of two sharp-mode couplings and their unusual momentum dependence in the superconducting state of $\text{Bi}_2\text{Sr}_2\text{CaCu}_2\text{O}_{8+\delta}$ revealed by laser-based angle-resolved photoemission, Phys. Rev. Lett. **111**, 107005 (2013).
- ⁹⁴ S.-L. Yang, J. A. Sobota, Y. He, D. Leuenberger, H. Soifer, H. Eisaki, P. S. Kirchmann, and Z.-X. Shen, Mode-selective coupling of coherent phonons to the $\text{Bi}2212$ electronic band structure, Phys. Rev. Lett. **122**, 176403 (2019).
- ⁹⁵ D. S. Dessau, Z. X. Shen, D. M. King, D. S. Marshall, L. W. Lombardo, P. H. Dickinson, A. G. Loeser, J. DiCarlo, C. H. Park, A. Kapitulnik, and W. E. Spicer, Key features in the measured band structure of $\text{Bi}_2\text{Sr}_2\text{CaCu}_2\text{O}_{8+\delta}$ flat bands at E_F and Fermi surface nesting, Phys. Rev. Lett. **71**, 2781 (1993).
- ⁹⁶ M. Eschrig and M. R. Norman, Neutron resonance: modeling photoemission and tunneling data in the superconducting state of $\text{Bi}_2\text{Sr}_2\text{CaCu}_2\text{O}_{8+\delta}$, Phys. Rev. Lett. **85**, 3261 (2000).
- ⁹⁷ D. Manske, I. Eremin, and K. H. Bennemann, Analysis of the elementary excitations in high- T_c cuprates: explanation of the new energy scale observed by angle-resolved photoemission spectroscopy, Phys. Rev. Lett. **87**, 177005 (2001).
- ⁹⁸ M. Eschrig and M. R. Norman, Dispersion anomalies in bilayer cuprates and the odd symmetry of the magnetic resonance, Phys. Rev. Lett. **89**, 277005 (2002).
- ⁹⁹ See, e.g., the review, M. Eschrig, The effect of collective spin-1 excitations on electronic spectra in high- T_c superconductors, Adv. Phys. **55**, 47 (2006).
- ¹⁰⁰ R. Mahajan, M. Barkeshli, and S. A. Hartnoll, Non-Fermi liquids and the Wiedemann-Franz law, Phys. Rev. B **88**, 125107 (2013).
- ¹⁰¹ S. A. Hartnoll, R. Mahajan, M. Punk, and S. Sachdev, Transport near the Ising-nematic quantum critical point of metals in two dimensions, Phys. Rev. B **89**, 155130 (2014).
- ¹⁰² A. A. Patel and S. Sachdev, dc resistivity at the onset of spin density wave order in two-dimensional metals, Phys. Rev. B **90**, 165146 (2014).
- ¹⁰³ A. Lucas and S. Sachdev, Memory matrix theory of magnetotransport in strange metals, Phys. Rev. B **91**, 195122 (2015).
- ¹⁰⁴ L. E. Vieira, V. S. de Carvalho, H. Freire, DC resistivity near a nematic quantum critical point: Effects of weak disorder and acoustic phonons, Ann. Phys. **419**, 168230 (2020).
- ¹⁰⁵ I. Mandal and H. Freire, Transport in the non-Fermi liquid phase of isotropic Luttinger semimetals, Phys. Rev. B **103**, 195116 (2021).
- ¹⁰⁶ R. E. Prange and L. P. Kadanoff, Transport theory for electron-phonon interactions in metals, Phys. Rev. **134**, A566 (1964).
- ¹⁰⁷ L. Kuang, Y. Lan, and S. Feng, Dynamical spin response in cuprate superconductors from low-energy to high-energy, J. Magn. Magn. Mater. **374**, 624 (2015).
- ¹⁰⁸ F. Yuan, S. Feng, Z. B. Su, and L. Yu, Doping and temperature dependence of incommensurate antiferromagnetism in underdoped lanthanum cuprates, Phys. Rev. B **64**, 224505 (2001).
- ¹⁰⁹ S. Feng and Z. Huang, Universal spin response in copper oxide materials, Phys. Rev. B **57**, 10328 (1998).
- ¹¹⁰ J. A. N. Bruin, H. Sakair, R. S. Perry, A. P. Mackenzie, Similarity of scattering rates in metals showing T -linear resistivity, Science **339**, 804 (2013).
- ¹¹¹ S. A. Grigera, R. S. Perry, A. J. Schofield, M. Chiao, S. R. Julian, G. G. Lonzarich, S. I. Ikeda, Y. Maeno, A. J. Millis, and A. P. Mackenzie, Magnetic field-tuned quantum criticality in the metallic ruthenate $\text{Sr}_3\text{Ru}_2\text{O}_7$, Science **294**, 329 (2001).
- ¹¹² X. Ma, M. Zeng, and S. Feng, unpublished.
- ¹¹³ Y. Mou, Y. Liu, S. Tan, and S. Feng, Doping and momentum dependence of coupling strength in cuprate superconductors, Phil. Mag. **99**, 2718 (2019).